Limitations on validating slitted sound absorber designs through budget additive manufacturing

Materials & Design 218 (2022) 110703

Contents lists available at ScienceDirect

Materials & Design

journal homepage: www.elsevier.com/locate/matdes

Limitations on validating slitted sound absorber designs through budget additive manufacturing

K.C. Opiela [a,*], T.G. Zieliński [a], K. Attenborough [b]

[a] Institute of Fundamental Technological Research, Polish Academy of Sciences, Pawińskiego 5B, 02-106 Warsaw, Poland
[b] The Open University, School of Engineering and Innovation, Milton Keynes MK7 6AA, UK

HIGHLIGHTS

- Slitted sound absorbers have primitive yet acoustically absorptive structure.
- Samples composed just of inclined slits cannot be measured in an impedance tube.
- Perforation and zigzags open up an inclined slit network of a cylindrical sample.
- Absorption predictions are compared with measurements made on 3D printed samples.
- Budget additive manufacturing yields geometrical imperfections in the samples.

GRAPHICAL ABSTRACT

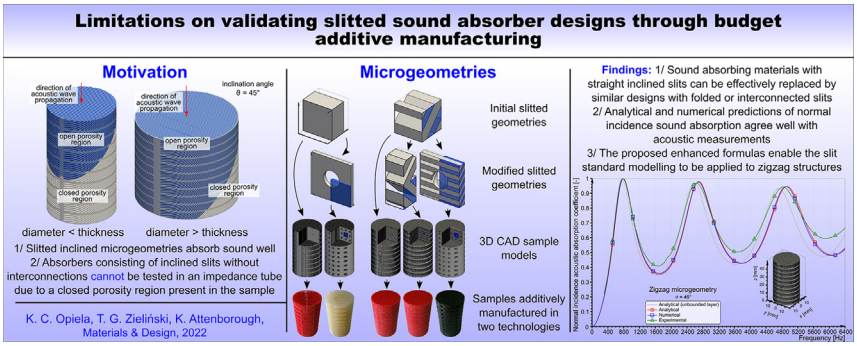

ARTICLE INFO

Article history:
Received 7 February 2022
Revised 18 April 2022
Accepted 27 April 2022
Available online 2 May 2022

Keywords:
Slitted sound absorber
Additive manufacturing
Microstructure-based modelling

ABSTRACT

The potential usefulness of relatively simple pore microstructures such as parallel, identical, inclined slits for creating broadband sound absorption has been argued through analytical models. In principle, such microstructures could be realised through budget additive manufacturing. However, validation of the analytical predictions through normal incidence impedance tube measurements on finite layers is made difficult by the finite size of the tube. The tube walls curtail the lengths of inclined slits and, as a result, prevent penetration of sound through the layer. As well as demonstrating and modelling this effect, this paper explores two manufacturing solutions. While analytical and numerical predictions correspond well to absorption spectra measured on slits normal to the surface, discrepancies between measured and predicted sound absorption are noticed for perforated and zigzag slit configurations. For perforated microgeometries this is found to be the case with both numerical and analytical modelling based on variable length dead-end pores. Discrepancies are to be expected since the dead-end pore model does not allow for narrow pores in which viscous effects are important. For zigzag slits it is found possible to modify the permeability used in the inclined slit analytical model empirically to obtain reasonable agreement with data.

1. Introduction

Absorption of a low-frequency sound is still a challenging problem. Apart from being effective, acoustic treatments are often designed to meet other important criteria like good thermal

* Corresponding author.
E-mail addresses: kopiela@ippt.pan.pl (K.C. Opiela), tzielins@ippt.pan.pl (T.G. Zieliński), keith.attenborough@open.ac.uk (K. Attenborough).

https://doi.org/10.1016/j.matdes.2022.110703
0264-1275/

insulation and low weight. Porous materials generally comply very well with these requirements and therefore seem to be a natural choice in many acoustic applications. The enhanced dissipation of acoustic wave energy, on the grounds of thermal and visco-inertial effects present therein, eventuates from their specific internal structure composed of fluid-saturated domains (that is pores) surrounded by solid walls of a skeleton [1]. It is the geometry and spatial distribution of pores that essentially control the dissipative phenomena occurring at the micro-scale level. In particular, the first sound absorption peak caused by the quarter wavelength resonance in hard-backed rigid-frame porous layers can be shifted to lower frequencies by modifying either the thickness of the layer or the effective wave number that pertains to its specific microstructure [2,3]. In this regard, a tortuous pore-network proves clearly beneficial since it yields an increased effective path length and hence a reduced effective speed of sound in the medium [2]. Thereby, the overall sound absorption in the material is improved while maintaining its thickness and weight.

Various porous geometries have been devised and studied so far, some of them being very popular on the market of products for noise and vibration damping. Among many more or less complex solutions that boost performance of acoustic treatments, especially at low audible frequencies, one finds fibrous [4–7], meta-porous [8,9] and multi-layer [10,11] materials, micro-slit metamaterials [12], granular media [13–15], and highly-porous polyurethane [16–19], polyolefin [20], polymeric with membranes [21], double-porosity [22,23] or metal foams [24–28]. Recently, considerable effort has been made to 3D print passive [29–34] and adaptable [35,36] structures. Moreover, additive manufacturing has been utilised to create modern acoustic devices [37] and structure-acoustic integrated cellular lattices [38]. On the other hand, researchers and engineers have also focused on much more primitive or conventional configurations, including rigid micro-rods [39–41], parallel cylinders of diameter 2 mm [42], honeycomb [43], annular [44] and slitted designs [45–48], as well as additively manufactured perforated plates with oblique circular openings [49]. Attenborough [2,3] reviewed the knowledge about the available simple ideas and showed (though only theoretically) that such microstructures may lead to absorptive characteristics better or at least comparable to those published for some intricate porous geometries. This paper confronts some of these propositions with reality.

Slits belong to the most primitive shapes exhibiting great potential that depends on their permeability. While the analytical model for sound absorption in a hard-backed array of vertical slits [2,3] has been validated by experiments carried out on samples with moderate characteristic dimensions [50], the estimation of acoustic properties for narrow, inclined, straight slits has not been verified with success based on impedance tube direct tests yet. Previous attempts to do so were able just to compare predictions and measurements valid for non-inclined and zigzag slits with good accuracy [51,52]. The main reason for that is the relative ease in their manufacturing. Straight oblique slits, albeit more efficient, need interconnections, otherwise the propagation of acoustic waves within the entire pore-network of a sample inserted into an impedance tube, and thus bounded by it, will be prohibited. This means that (much larger) samples of such materials can only be tested in reverberation chambers, because in the case of testing in an impedance tube only slits originating at the insonified surface participate in airborne visco-thermal energy losses. In addition to a more elaborate microstructure due to interlinks, very thin inclined solid strips separating individual straight slits have a tendency to deform and stick together making their fabrication cumbersome too.

This contribution provides experimental and numerical (finite-element) verification of the theoretical approaches presented in [2,3] to the modelling of sound absorbers with narrow slits. Along with the simplest geometries studied in [2,3], it deals with more complex slit-like pore shapes that reflect profitable properties (for example, lower permeability) of inclined straight slits and, because of interconnected pores, make measurements of the corresponding samples in an impedance tube reasonable. As a continuation of the work reported in [51,52], the paper shows the current production capacity regarding the materials with slit widths and solid strip thicknesses of the order of tenths of a millimetre. Such small slit dimensions are at the limit of the manufacturing capabilities of the most commonly used budget 3D printing technologies today, such as Fused Deposition Modelling (FDM) or Photopolymerisation exploiting a liquid–crystal display (LCD) [53]. With a view to this, it is crucial to deploy appropriate equipment and input materials (low-shrinkage polymer filaments, low-viscosity photocurable resins, etc.) as well as numerous adjusted process settings to finally fabricate specimens of high quality. In contrast with the conference papers [51,52], this thoroughly elaborated contribution deals with new microgeometrical dimensions as well as new samples manufactured in two additive technologies, and includes novel approaches to the modelling of sound propagation in perforated and zigzag slits. Its objective is to provide normal incidence impedance tube results and their predictions obtained on shapes similar to the inclined straight slits and therefore indirectly validate models for straight inclined slits.

The paper concerns the producibility and performance of slitted sound absorbers. Sec. 2.1 describes the investigated periodic microgeometries. Sec. 2.2 and A provide a complete set of formulas applied to analytically and semi-analytically predict the absorption of acoustic wave energy within the specimens. Additive manufacturing and testing in an impedance tube of the prepared samples are explained in Sec. 2.3. The computational as well as experimental results are compared and discussed in Sec. 3. It is also where an analytical model valid for straight slits is empirically adapted to folded slits. At the end, main observations and original findings of the work are summarised.

2. Materials and methods

2.1. Slitted geometries

The most primitive regular slitted microgeometries are characterised by three parameters, that is the slit width $2w_s$, the thickness $2w_w$ of a solid strip separating two adjacent slits (that is the edge-to-edge spacing), and the inclination angle ϑ defined as the angle between the slit symmetry plane and a reference direction (in this work it is the direction of sound wave incidence); see Fig. 1. Consequently, the open porosity of a material is $\phi = w_s/(w_s + w_w)$. In more complex configurations, slits may be, for example, interconnected by cylindrical perforation channels of diameter d_{perf} or have a zigzag shape. In the former case the perforation should be regularly spaced on a grid with size l_{perf} to preserve periodicity. The latter situation means that slits fold every l_{fold} distance being constantly inclined at angle ϑ.

The slit dimensions and edge-to-edge spacings for the most effective slitted sound absorbers should be of the order of microns [2,3]. This is in fact beyond current capabilities in budget additive manufacturing. However, five microstructures yielding potentially useful sound absorbing properties have been developed using the smallest slit widths feasible with the low-cost manufacturing methods to hand. The designs can be classified into two groups with respect to the angle of incidence:

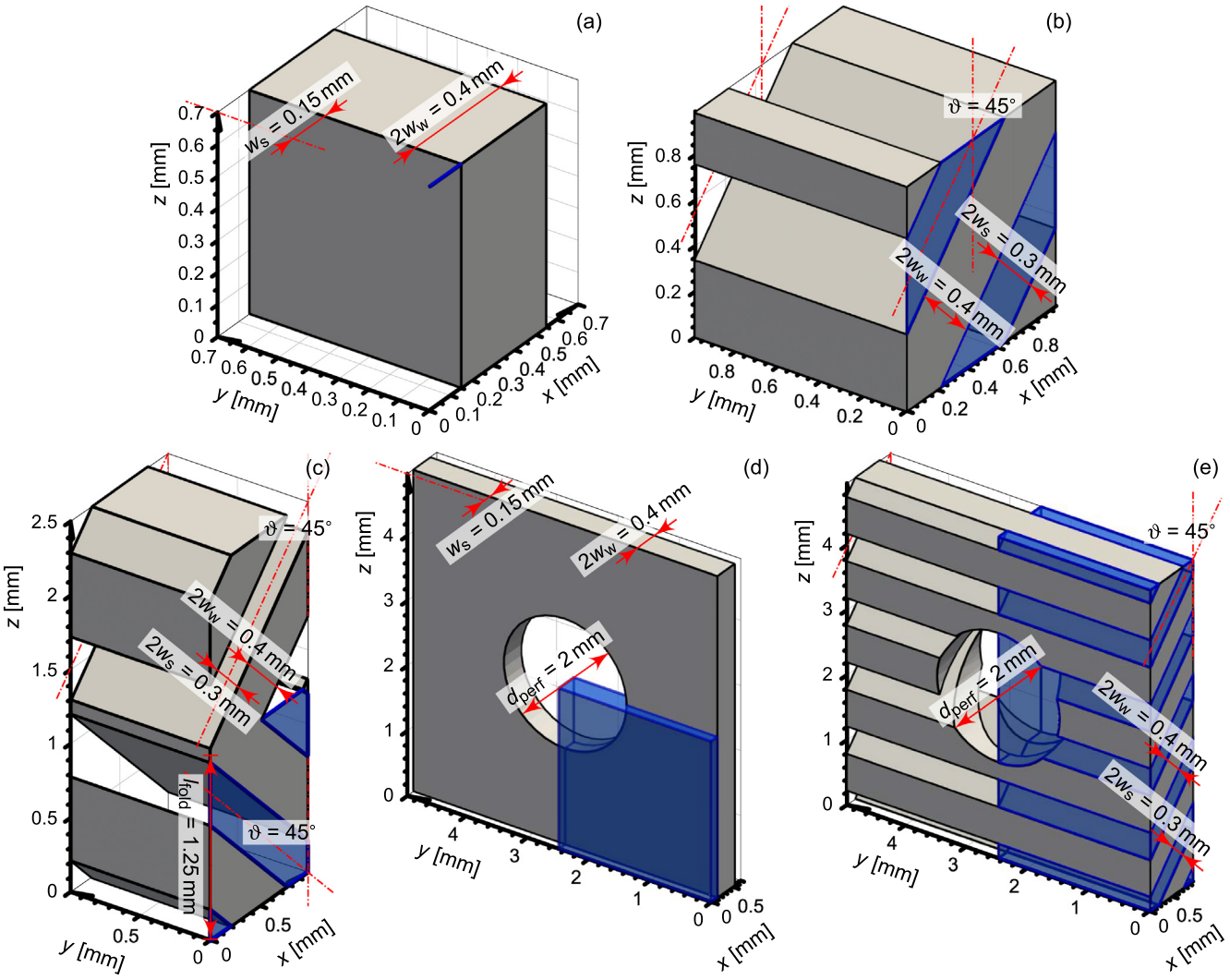

Fig. 1. The designed unit cell microgeometries: the uniformly slitted periodic structure with (a) $\vartheta = 0°$; (b) $\vartheta = 45°$ and no additional modification; (c) $\vartheta = 45°$ and a fold every 1.25 mm (zigzag); (d) $\vartheta = 0°$ and a cylindrical pore (perforation); (e) $\vartheta = 45°$ and a cylindrical pore (perforation). The blue region in each subfigure highlights the representative computational fluid domain used in numerical simulations.

1. Parallel, uniform, straight, non-inclined (that is with the inclination angle $\vartheta = 0°$) slits of width $2w_s = 0.3$ mm separated by solid strips of thickness $2w_w = 0.4$ mm (nominal porosity $\phi \approx 0.43$):
   (a) pure configuration—see Fig. 1a;
   (b) configuration with a periodic arrangement of cylindrical channels (perforation) of diameter $d_{perf} = 2$ mm and period $l_{perf} = 10(w_s + w_w)/\sin 45° \approx 4.95$ mm, perpendicular to the slit plane (resulting porosity $\phi \approx 0.5$)—see Fig. 1d.
2. Parallel, uniform slits of width $2w_s = 0.3$ mm separated by solid strips of thickness $2w_w = 0.4$ mm (nominal porosity $\phi \approx 0.43$) with the inclination angle $\vartheta = 45°$ and:
   (a) no other modifications—see Fig. 1b;
   (b) a zigzag shape with a fold every $l_{fold} = 1.25$ mm in the direction of incidence (along the z-axis)—see Fig. 1c;
   (c) a periodic perforation with cylindrical channels of diameter $d_{perf} = 2$ mm and period $l_{perf} = 10(w_s + w_w)/\sin\vartheta \approx 4.95$ mm, inclined to the slit plane at angle 45°, that is perpendicular to the direction of incidence (resulting porosity $\phi \approx 0.5$)—see Fig. 1e.

Fig. 1 presents periodic fragments of the devised skeletons (the so-called unit cells) that fully represent each considered material. Moreover, each subfigure shows a minimal representative computational fluid domain used in the numerical simulations discussed in Sec. 3. Fig. 1b illustrates a unit cell composed of just inclined slits, equivalent to those shown in Figs. 1c and e, but without the fold and perforation, respectively. This microstructure effectively precludes sound wave propagation within the entire volume of an associated specimen placed inside an impedance tube due to the lack of interconnections between adjacent pores. Nevertheless, it was used as the reference microgeometry for all results involving oblique slits. To be able to experimentally reflect the acoustic properties of the material composed of ideal, straight, inclined slits from Fig. 1b, the zigzags and 2-mm perforations (Figs. 1c and e, respectively) were designed. They minimise the risk of closed pores being present in the manufactured samples, and guarantee that the printing process is feasible and accurate. The cylindrical channel with diameter $d_{perf} = 2$ mm was also added to the slitted structure with $\vartheta = 0°$ (Fig. 1d) for the sake of completeness, although in this case it was not necessary as the incident acoustic waves propagating in the z-direction can penetrate to every slit in the 3D printed material sample inserted to an impedance tube—all slits are physically linked together by the fluid region in front of the specimen.

2.2. Sound absorption prediction for slitted materials

The sound absorption coefficient is one of the basic acoustic descriptors as it states what is the ratio of the wave energy absorbed by a material layer to incident energy. It varies from 0 to 1 for no attenuation and perfect absorption, respectively, and can be predicted analytically and numerically using the equivalent-fluid approach for rigid-frame porous media [1,54]. The method relies on substituting the investigated open-porosity medium by a homogenised equivalent fluid that accurately mirrors its macroscopic acoustic properties expressed in the equivalent density, $\varrho_{\mathrm{eq}}(\omega)$, and equivalent bulk modulus, $K_{\mathrm{eq}}(\omega)$, where $\omega = 2\pi f$ is the angular frequency and time dependence $\exp(-\mathrm{i}\omega t)$ is understood (i is the imaginary unit, t is time, f is the temporal frequency). These frequency-dependent complex-valued functions are calculated from the dynamic visco-inertial, $\alpha(\omega)$, and dynamic thermal, $\alpha'(\omega)$, tortuosities, respectively, and from properties of the fluid saturating the pores. When it is air, the relations read:

$$\varrho_{\mathrm{eq}}(\omega) = \frac{\varrho_{\mathrm{air}}\alpha}{\phi} \tag{1}$$

and

$$K_{\mathrm{eq}}(\omega) = \frac{K_{\mathrm{air}}}{\phi}\left(\gamma_{\mathrm{air}} - \frac{\gamma_{\mathrm{air}}-1}{\alpha'}\right)^{-1}, \tag{2}$$

where $\varrho_{\mathrm{air}} = 1.204\,\mathrm{kg/m^3}$ denotes the density of air, $K_{\mathrm{air}} = 141855\,\mathrm{Pa}$ is its bulk modulus, and $\gamma_{\mathrm{air}} = 1.4$ is the ratio of specific heats (the adiabatic index) for air. Based on the assumption of plane wave fronts with normal incidence and utilising the equivalent properties, the acoustic wave propagation in such dispersive media on the macroscale level is described by the Helmholtz equation of time-harmonic linear acoustics. Consequently, the surface acoustic impedance, $Z_{\mathrm{s}}(\omega)$, for a single porous layer of thickness H_{s} with rigid termination is written analytically as [1,54]:

$$Z_{\mathrm{s}}(\omega) = -\mathrm{i}Z_{\mathrm{eq}}\cot\left(\omega H_{\mathrm{s}} c_{\mathrm{eff}}^{-1}\right) \tag{3}$$

and transforms to the transfer matrix formula:

$$\begin{aligned} Z_{\mathrm{s}}(\omega) &= Z_{\mathrm{eq}}\frac{Z_{\mathrm{eq}} - \mathrm{i}Z_{\mathrm{g}}\cot(\omega H_{\mathrm{s}} c_{\mathrm{eff}}^{-1})}{Z_{\mathrm{g}} - \mathrm{i}Z_{\mathrm{eq}}\cot(\omega H_{\mathrm{s}} c_{\mathrm{eff}}^{-1})}, \\ Z_{\mathrm{g}}(\omega) &= -\mathrm{i}Z_{\mathrm{air}}\cot(\omega H_{\mathrm{g}} c_{\mathrm{air}}^{-1}) \end{aligned} \tag{4}$$

for a system comprised of an air layer of thickness H_{g} placed in between a porous layer and the hard-backing (see Fig. 6). In Eqs 3 and 4, $Z_{\mathrm{eq}}(\omega) = \sqrt{\varrho_{\mathrm{eq}}K_{\mathrm{eq}}}$ is the equivalent characteristic impedance, whereas $c_{\mathrm{eff}}(\omega) = \sqrt{K_{\mathrm{eq}}/\varrho_{\mathrm{eq}}}$ is the effective speed of sound in the homogenised medium that replaces the porous layer. The formulation of the transfer matrix method for an arbitrary acoustic system is explained, for example, in [55]. Knowing $Z_{\mathrm{s}}(\omega)$ as well as the characteristic impedance of the pore-fluid, $Z_{\mathrm{air}} = \sqrt{\varrho_{\mathrm{air}}K_{\mathrm{air}}}$, the real-valued acoustic absorption coefficient, $\mathscr{A}(\omega)$, can be determined from the classic expression [1,54]:

$$\mathscr{A}(\omega) = 1 - \left|\frac{Z_{\mathrm{s}} - Z_{\mathrm{air}}}{Z_{\mathrm{s}} + Z_{\mathrm{air}}}\right|^2. \tag{5}$$

The procedure leading to the computation of the normal incidence sound absorption coefficient of a porous layer with a rigid frame is illustrated in Fig. 2.

2.2.1. Analytical model for inclined slits

The sound absorption in porous materials can be predicted analytically, provided that their microstructure is extremely simple. For the considered slitted, air-saturated samples the analytical approximations of the dynamic tortuosities, $\alpha_{\mathrm{A}}(\omega)$ and $\alpha\prime_{\mathrm{A}}(\omega)$, are [2,3]:

$$\alpha_{\mathrm{A}}(\omega) = \cos^{-2}\vartheta\left(1 - \frac{\tanh(\lambda\sqrt{\mathrm{i}})}{\lambda\sqrt{\mathrm{i}}}\right)^{-1}, \tag{6}$$

$$\alpha\prime_{\mathrm{A}}(\omega) = \left(1 - \frac{\tanh(\lambda\sqrt{\mathrm{i}N_{\mathrm{Pr,air}}})}{\lambda\sqrt{\mathrm{i}N_{\mathrm{Pr,air}}}}\right)^{-1}, \tag{7}$$

where $\lambda(\omega) = w_{\mathrm{s}}\sqrt{\omega\varrho_{\mathrm{air}}/\mu_{\mathrm{air}}}$, $N_{\mathrm{Pr,air}} = 0.71$ is the Prandtl number for air, and $\mu_{\mathrm{air}} = 18.27\cdot 10^{-6}\,\mathrm{Pa\cdot s}$ is the dynamic viscosity of air. The above estimations are very useful since one needs to specify merely two model parameters—w_{s} and ϑ—to calculate $\alpha_{\mathrm{A}}(\omega)$ and $\alpha\prime_{\mathrm{A}}(\omega)$. The information about the porosity or slit spacing is not required at this stage.

2.2.2. Analytical model for slits with cylindrical perforation

Following Leclaire, Umnova, Dupont, and Panneton [56], one can express the equivalent density and bulk modulus of the perforated slitted material in terms of their main-pore (superscript 'M') and side-pore (superscript 'S') contributions:

$$\varrho_{\mathrm{eq}}(\omega) = \varrho_{\mathrm{eq}}^{\mathrm{M}} = \frac{\varrho_{\mathrm{air}}\alpha_{\mathrm{A}}^{\mathrm{M}}}{\phi^{\mathrm{M}}}, \tag{8}$$

$$K_{\mathrm{eq}}(\omega) = \frac{1}{\phi^{\mathrm{M}}}\left(\left(\phi^{\mathrm{M}}K_{\mathrm{eq}}^{\mathrm{M}}\right)^{-1} + \left(\phi^{\mathrm{S}}K_{\mathrm{eq}}^{\mathrm{S}}\right)^{-1}\frac{N^{\mathrm{S}}h^{\mathrm{S}}}{l^{\mathrm{S}}}\frac{A^{\mathrm{S}}}{A^{\mathrm{M}}}\tan\left(\frac{\omega h^{\mathrm{S}}}{c_{\mathrm{eff}}^{\mathrm{S}}}\right)\frac{c_{\mathrm{eff}}^{\mathrm{S}}}{\omega h^{\mathrm{S}}}\right)^{-1}, \tag{9}$$

where $N^{\mathrm{S}} = 2$ is the number of side branches (that is perforation channels) per unit cell, $h^{\mathrm{S}} = w_{\mathrm{w}}$ is the length of side branches, $l^{\mathrm{S}} = l_{\mathrm{perf}}$ is the spacing of side branches, $A^{\mathrm{S}} = \frac{1}{4}\pi d_{\mathrm{perf}}^2$ is the cross-section area of cylindrical side branches, $A^{\mathrm{M}} = 2w_{\mathrm{s}}l^{\mathrm{S}}$ is the cross-section area of main slits per unit cell, ϕ^{M} is the volume fraction of main slits, ϕ^{S} is the volume fraction of side branches (in other words, perforation rate), $c_{\mathrm{eff}}^{\mathrm{S}}(\omega) = \sqrt{K_{\mathrm{eq}}^{\mathrm{S}}/\varrho_{\mathrm{eq}}^{\mathrm{S}}}$ is the effective speed of sound in side branches, $\alpha_{\mathrm{A}}^{\mathrm{M}} = \alpha_{\mathrm{A}}$, and $K_{\mathrm{eq}}^{\mathrm{M}} = K_{\mathrm{air}}/(\phi^{\mathrm{M}}(\gamma_{\mathrm{air}} - (\gamma_{\mathrm{air}}-1)/\alpha\prime_{\mathrm{A}}))$. $K_{\mathrm{eq}}^{\mathrm{S}}$ and $\varrho_{\mathrm{eq}}^{\mathrm{S}}$ are computed using the analytical formulas for cylindrical pores involving the Bessel functions of the first kind of zero and first order, denoted $J_0(\xi)$ and $J_1(\xi)$, respectively [2,3]:

$$\varrho_{\mathrm{eq}}^{\mathrm{S}}(\omega) = \frac{\varrho_{\mathrm{air}}}{\phi^{\mathrm{S}}}G^{-1}\left(\frac{d_{\mathrm{perf}}}{2}\sqrt{\frac{\omega\varrho_{\mathrm{air}}}{\mu_{\mathrm{air}}}}\right), \tag{10}$$

$$K_{\mathrm{eq}}^{\mathrm{S}}(\omega) = \frac{K_{\mathrm{air}}}{\phi^{\mathrm{S}}}\left(\gamma_{\mathrm{air}} - (\gamma_{\mathrm{air}}-1)G\left(\frac{d_{\mathrm{perf}}}{2}\sqrt{N_{\mathrm{Pr,air}}\frac{\omega\varrho_{\mathrm{air}}}{\mu_{\mathrm{air}}}}\right)\right)^{-1}, \tag{11}$$

where $G(\xi) = 1 - 2J_1\left(\xi\sqrt{-\mathrm{i}}\right)/\left(\xi\sqrt{-\mathrm{i}}J_0\left(\xi\sqrt{-\mathrm{i}}\right)\right)$.

According to the presented model only thermal effects in side branches contribute to the overall sound energy dissipation within the material because visco-inertial losses are negligible. Because the thermal phenomena taking place within the pores are *not* directional, $K_{\mathrm{eq}}(\omega)$ can equivalently be evaluated by treating the cylindrical perforations as the main pore network, and assuming that the slits are the dead-end pores. As a result, $\varrho_{\mathrm{eq}}(\omega)$ does not change, while $K_{\mathrm{eq}}(\omega)$ takes the form (9) with $N^{\mathrm{S}} = 1, h^{\mathrm{S}} \approx l_{\mathrm{perf}}/2, l^{\mathrm{S}} = 2(w_{\mathrm{s}} + w_{\mathrm{w}}), A^{\mathrm{S}} = 2w_{\mathrm{s}}l_{\mathrm{perf}}$, and $A^{\mathrm{M}} = \frac{1}{4}\pi d_{\mathrm{perf}}^2$. If this approach is adopted, one must carefully estimate the length of side branches h^{S} as the slit length varies due to the cylindrical shape of the sample so that the slits close to its central axis are longer than those localised far from it. To differentiate between the two variants, the former is called 'dead-end perforation' model and the latter 'dead-end slit' model.

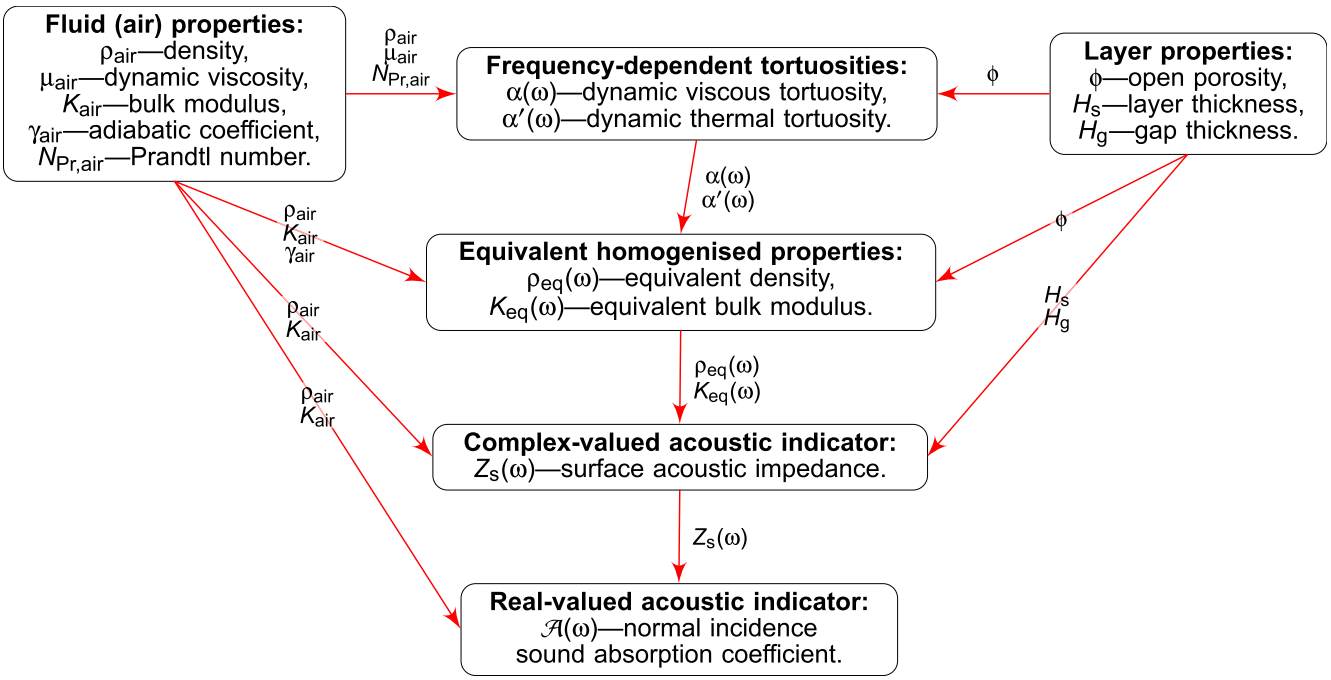

Fig. 2. Properties and quantities used for sound absorption prediction.

2.2.3. Numerical model

Alternatively, there exist more complex equivalent-fluid models for rigid-frame porous materials with a more arbitrary microstructure. One of them—the Johnson-Champoux-Allard-Lafarge-Pride (JCALP) model [57–62]—estimates the 'numerical' dynamic tortuosities, $\alpha_{\mathrm{N}}(\omega)$ and $\alpha\prime_{\mathrm{N}}(\omega)$, by means of eight geometry-based parameters:

- open porosity, ϕ,
- static viscous permeability, k_0,
- static thermal permeability, $k\prime_0$,
- (kinematic) tortuosity, α_∞,
- static viscous tortuosity, α_0,
- static thermal tortuosity, $\alpha\prime_0$,
- viscous characteristic length, Λ, and
- thermal characteristic length, Λ'.

The corresponding expressions read:

$$\alpha_{\mathrm{N}}(\omega)=\alpha_\infty+\frac{\mu_{\mathrm{air}}}{\mathrm{i}\omega\varrho_{\mathrm{air}}}\frac{\phi}{k_0}\left(\sqrt{\frac{\mathrm{i}\omega\varrho_{\mathrm{air}}}{\mu_{\mathrm{air}}}\left(\frac{2\alpha_\infty k_0}{\Lambda\phi}\right)^2+b^2}-b+1\right),$$

$$b=\frac{2{\alpha_\infty}^2 k_0}{\Lambda^2\phi(\alpha_0-\alpha_\infty)}, \tag{12}$$

$$\alpha\prime_{\mathrm{N}}(\omega)=1+\frac{\mu_{\mathrm{air}}}{\mathrm{i}\omega\varrho_{\mathrm{air}}N_{\mathrm{Pr,air}}}\frac{\phi}{k\prime_0}\left(\sqrt{\frac{\mathrm{i}\omega\varrho_{\mathrm{air}}N_{\mathrm{Pr,air}}}{\mu_{\mathrm{air}}}\left(\frac{2k\prime_0}{\Lambda'\phi}\right)^2+b'^2}-b'+1\right),$$

$$b'=\frac{2k\prime_0}{\Lambda\prime^2\phi(\alpha\prime_0-1)}. \tag{13}$$

The subscripts '0' and '∞' refer to quantities associated with low- ($\omega\to 0$) or high-frequency ($\omega\to\infty$) limits, respectively. This multi-scale approach is sometimes called 'hybrid' because the required parameters are often evaluated numerically on a unit cell representative for the porous microstructure of a given medium. This is also why the qualifier 'numerical' and subscript 'N' are assigned to the dynamic tortuosities $\alpha_{\mathrm{N}}(\omega)$ and $\alpha\prime_{\mathrm{N}}(\omega)$. While both ϕ and Λ' are determined directly from the microgeometry, the remaining parameters, namely k_0,$k\prime_0$,α_∞,α_0, $\alpha\prime_0$ and Λ, are taken from the solutions to three steady-state boundary value problems formulated in the fluid domain at the microscale level [54]:

1. the Stokes flow through a unit cell driven by a unit pressure gradient acting in the direction of acoustic wave propagation with the no-slip boundary condition set on solid walls—the Stokes problem;
2. an electric conduction problem in a pore-fluid with a non-conducting skeleton caused by the application of a uniform, dimensionless, unit (electric) vector field in the direction of incidence—the Laplace problem;
3. a thermal diffusion produced by a uniform, dimensionless, unit heat source inside the fluid with the isothermal boundary condition imposed on solid surfaces—the Poisson problem.

The corresponding equations and formulas are briefly recalled in App. A.

The JCALP model is the most advanced from the family that also includes the so-called Johnson-Champoux-Allard (JCA) and Johnson-Champoux-Allard-Lafarge (JCAL) models. The latter two are frequently employed because the required parameters (five and six, respectively) are relatively easily measurable and often sufficient for correct predictions. However, due to inherent limitations of the JCA and JCAL models, their application is restricted to non-uniform porous networks without abrupt bottlenecks [1]. Since some of the microgeometries of interest are quite complicated, it is more appropriate to use the JCALP model in this work, as it accounts for pores with possible constrictions between them, like the 2-mm perforation channel intersected by the 0.3 mm-wide slit.

2.3. Manufacturing and acoustic testing of material samples

Apart from being predicted, sound absorption by a layer comprised of the microgeometies introduced in Sec. 2.1 can be deduced from acoustic pressure measurements made in an impedance tube on a 3D printed material sample. To do so, each of the periodic unit

cells illustrated in Fig. 1 was contiguously arranged in a rectangular three-dimensional array, which was then virtually cut into a cylindrical shape in the FreeCAD freeware [63]. In such a manner five computer-aided design (CAD) models of cylindrical material samples with diameter of $D_s \cong 29\,\text{mm}$ and thickness of $H_s = 49.5\,\text{mm} \approx 10 l_{\text{perf}}$ were generated. Fig. 3 shows the appearance of porous CAD models as well as a unit-cell composition of each of them. Ten narrow clamping rings (about 0.4 mm-wide and 1 mm-thick) evenly distributed on the specimen circumference (see Figs. 3a, b and c), or a 0.3-mm solid wall laterally surrounding the sample (see Figs. 3d and e) were especially prepared to assure equal distances between slits throughout the specimen, their rigidity and proper fixation.

The slitted three-dimensional computer models were sliced in a dedicated software (Slic3r Prusa [64] and Z-SUITE [65] for the FDM and LCD processes, respectively) and additively manufactured in the Fused Deposition Modelling and Photopolymerisation technologies [53] from an acrylonitrile butadiene styrene filament by rigid.ink (the samples in Figs. 4a, b, and c), and low-viscosity (about $50\,\text{mPa}\cdot\text{s}$ at 25 °C) polymer, photocurable Zortrax Basic Pigment-free and Zortrax Pro Black resins (the samples in Figs. 4d and e), respectively. A low-cost FDM machine (FlashForge Creator Pro) equipped with a 0.4-mm nozzle and a heated bed (90 °C) was utilised. The FDM process consists of melting at 230 °C and extruding in a closed environment a continuous material layer-by-layer to build a final object. The more-demanding, inclined microstructures were printed on the Zortrax Inkspire device in the more advanced LCD technology in which a thin layer of a liquid resin is exposed to the UV light (emitted from a liquid–crystal display) and selectively cured on a platform to form a designed shape. The working platform is repeatedly lifted in the z-direction by a single component layer thickness, and a new cross-section pattern is cured until the whole object is complete. Due to differences in the production process itself, the LCD samples were obtained with a 0.025-mm component layer thickness, compared to 0.08-mm for FDM. Supports other than reinforcing rings or walls were not created in either case and the samples were printed along their central axis (thus were self-supporting). The LCD technology is generally considered as providing better quality printouts than FDM, but since it uses a viscous resin as a feedstock that one needs to remove from pores in an isopropanol bath after finishing the manufacturing process, FDM is supposedly more appropriate for printing narrow slits without interconnections. The information about the specimen fabrication is summarised in Table 1.

The overall quality of each printout was examined with the help of a digital microscope. Fig. 5 presents the determined characteristic dimensions of some of the manufactured geometries. It was

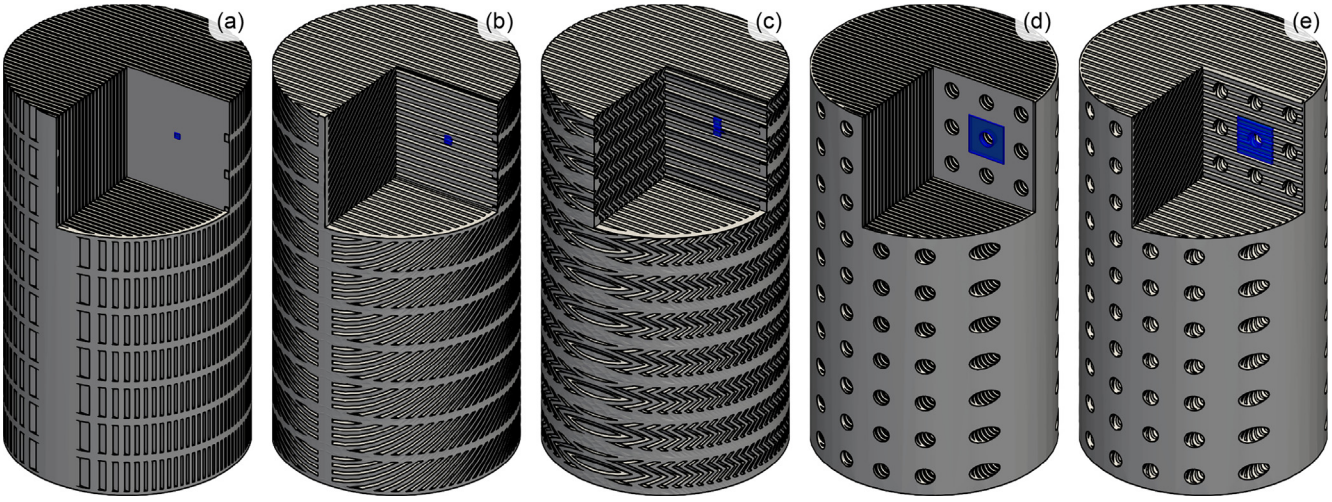

Fig. 3. CAD geometries of the generated cylindrical material samples ($D_s \cong 29\,\text{mm}$ and $H_s = 49.5\,\text{mm}$): the uniformly slitted sample with (a) $\vartheta = 0°$; (b) $\vartheta = 45°$ and no additional modification; (c) $\vartheta = 45°$ and a fold every 1.25 mm (zigzag); (d) $\vartheta = 0°$ and the cylindrical perforation; (e) $\vartheta = 45°$ and the cylindrical perforation. In each subfigure a corner region was virtually removed to show the corresponding unit cell from Fig. 1 (in blue). (For interpretation of the references to colour in this figure legend, the reader is referred to the web version of this article.)

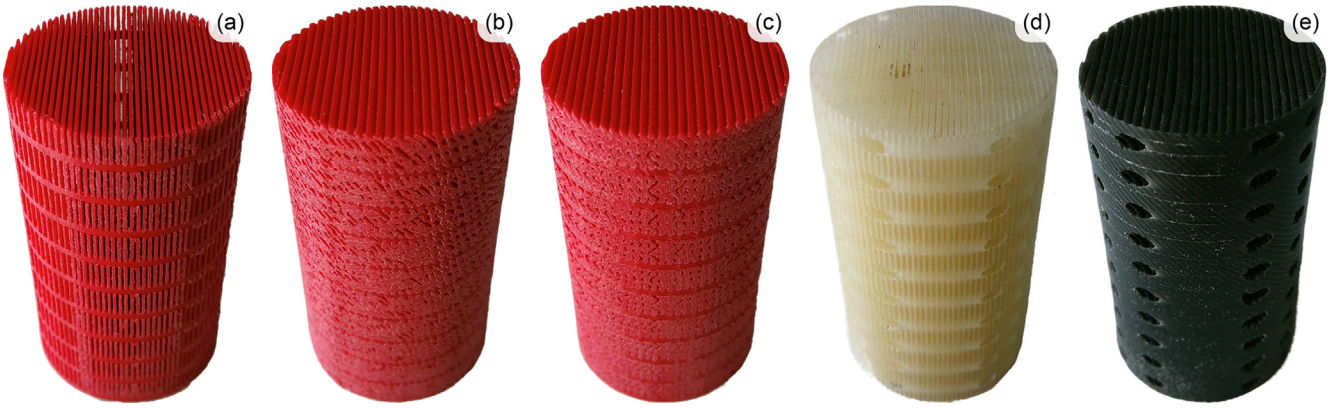

Fig. 4. Photographs of additively manufactured cylindrical material samples ($D_s \cong 29\,\text{mm}$ and $H_s = 49.5\,\text{mm}$): the uniformly slitted sample with (a) $\vartheta = 0°$; (b) $\vartheta = 45°$ and no additional modification; (c) $\vartheta = 45°$ and a fold every 1.25 mm (zigzag); (d) $\vartheta = 0°$ and the cylindrical perforation; (e) $\vartheta = 45°$ and the cylindrical perforation.

Table 1
Manufacturing technologies and 3D printing devices used.

Feature	Additive technology	
	Fused Deposition Modelling	LCD Photopolymerisation
Device	FlashForge Creator Pro	Zortrax Inkspire
Max built volume	230 × 150 × 155 mm	132 × 74 × 175 mm
Slicing software	Slic3r Prusa [64]	Z-SUITE [65]
Material	acrylonitrile butadiene styrene (rigid.ink ABS)	polymer photocurable resin (Zortrax Basic Pigment-free and Zortrax Pro Black)
Component layer thickness	0.08 mm	0.025 mm
Nozzle diameter	0.4 mm	–
Pixel size	–	0.05 mm
Filament diameter	1.75 mm	–
Wavelength	–	405 nm
Supports	not used	not used
Postprocessing	no	yes (isopropanol bath, heating and UV curing)

observed that the designed ideal shapes and sizes are reflected fairy well at the top and lateral surfaces of the samples, with the intended dimensions (w_s,w_w,d_{perf}, and l_{perf}) being largely preserved. The identified discrepancies are probably related to the imprecise measurements caused by the blurred edges or optical distortion (perspective) in the photographs. Nevertheless, it is visible in Figs. 5b and c that the 3D printouts have rough surfaces and that solid strips in the LCD samples are slightly buckled. Little degeneration of slits, especially in their inner parts deep inside the specimens, may also be captured while looking at the top surface of the LCD samples against the light with the naked eye. However, it is hard to quantify these shape imperfections because some solid strips are mildly twisted, and some are regular and straight as in the FDM samples.

The absorption of acoustic waves in the slitted structures shown in Fig. 4 was investigated both computationally and experimentally. A 29-mm Brüel & Kjær impedance tube was used to carry out acoustic measurements on the manufactured samples for frequencies f ranging between 300 Hz and 6.4 kHz. The frequency-dependent sound absorption coefficient was determined from the readings of acoustic pressure levels at two specified positions inside the tube in accordance with the two-microphone transfer function method [66]. Correct operation of the experimental equipment, detailed in Table 2, has been recently validated by a round robin test [34]. The 49.5 mm-thick well-fitted specimens were considered alone and with an air gap of thickness $H_g = 10.5$ mm introduced between the sample and the terminating rigid piston. Small radial dimensions of the reinforcing circumferential rings and walls added to the additively manufactured specimens (see Figs. 3 and 4 as well as Figs. 5b and c) were found to have little influence on the results, and were thus neglected in

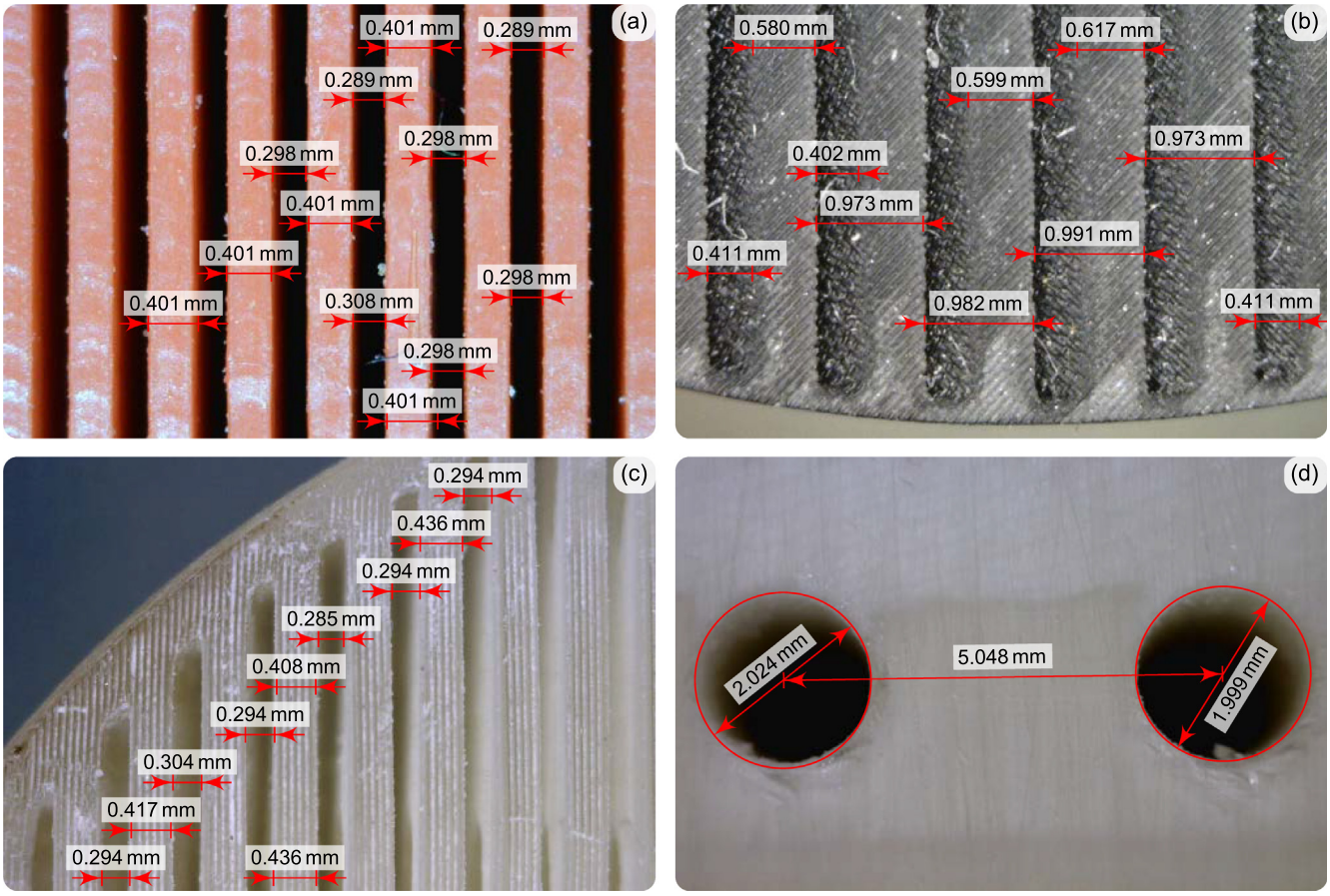

Fig. 5. Microscope measurements of the characteristic dimensions of the manufactured slitted microgeometries with: (a) $\vartheta = 0^\circ$ (top view of the sample); (b) $\vartheta = 45^\circ$ and the cylindrical perforation (top view of the sample); (c) $\vartheta = 0^\circ$ and the cylindrical perforation (top view of the sample); and (d) $\vartheta = 0^\circ$ and the cylindrical perforation (side view of the sample). The designed values are: $2w_s = 0.3$ mm and $2w_w = 0.4$ mm in (a, c), $2w_s/\cos\vartheta \approx 0.424$ mm and $2w_w/\cos\vartheta \approx 0.566$ mm in (b), and $d_{perf} = 2$ mm and $l_{perf} \approx 4.95$ mm in (d).

Table 2
Specification of the experimental setup.

Feature	Specification
Impedance tube	Brüel & Kjær Type 4206
Impedance tube diameter	29 mm
Nominal measurement range	500 Hz to 6.4 kHz
Operating principle	two-microphone transfer function method [66]
Software	Brüel & Kjær PULSE LabShop v15.1.0.15
Microphones	Brüel & Kjær Type 4187
Signal	white noise
Signal generator	Rigol DG1022
Data acquisition hardware	Brüel & Kjær LAN XI Module Type 3050-A-060

calculations. A schematic impedance tube configuration being studied is depicted in Fig. 6.

Impedance tube measurements based on normal incidence plane acoustic waves are typically conducted on macroscopically homogeneous porous specimens like conventional acoustic treatments with more or less complicated microstructure. Problems arise when using them for idealised simple structures or materials 3D printed on budget devices due to comparatively large characteristic dimensions. During the measurement a sample is backed by a rigid termination (or an air gap and a rigid termination) on the other side of the tube than a loudspeaker generating white noise is mounted (see Fig. 6). Then, the acoustic pressure is read in two specified locations in the impedance tube, collected by a data acquisition hardware and the so-called two-microphone transfer function method is utilised to calculate the surface acoustic impedance and sound absorption coefficient spectra from the pressure values and other data. The smaller the tube diameter, the wider the operating frequency range and the smaller the distance between the two microphones and between the first microphone and the incident surface of a sample.

3. Results and discussion

The numerical and analytical techniques based on the formulas given in Sec. 2.2 were deployed to determine the sound propagation and attenuation phenomena in the fabricated material samples. Three-, two-, and one-dimensional microscopic numerical analyses, with dimensions reduced due to the correlation between the symmetry of a computational domain and a specific propagation direction, were performed using the finite element method [67,68]. Dense computational meshes refined near solid walls were generated on the minimal representative domains (see the blue regions in Fig. 1) for each microstructure in Gmsh [69], and the appropriate boundary conditions for each analysis were set (see an exemplary mesh with the boundary conditions shown in

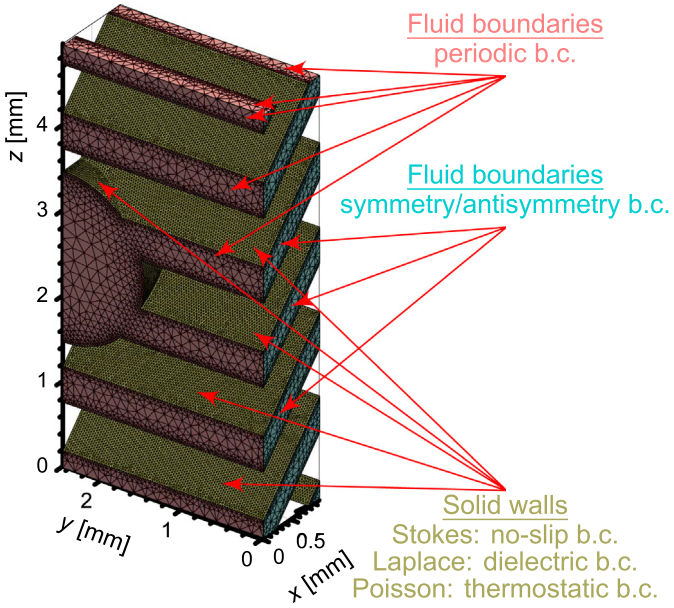

Fig. 7. Exemplary finite-element mesh with the applied boundary conditions (also on the invisible sides) for the slitted microstructure with $\vartheta = 45°$ and the cylindrical perforation presented in Fig. 1e. Note that the results included in the paper were obtained on a finer mesh that would not be legible if shown in the figure instead.

Fig. 7). The corresponding linear problems with up to about eight million degrees of freedom were solved in parallel on a machine with four CPU cores and 32 GB of a random-access memory by the aid of the FEniCS v2019.1.0 open-source library [67]. The software and the procedures presented in Sec. 2.2 and A were implemented in Python. Basic finite-element data for all the conducted numerical analyses and created 1D, triangular or tetrahedral meshes are summarised in Table 3. Their results served the calculation of the 'numerical' curves included in the following graphs.

Fig. 8 shows the normal incidence sound absorption coefficient spectra for the studied non-perforated and non-inclined slitted geometry. The predictions are confirmed very well by acoustic measurements made on the 3D printed sample, at least for frequencies up to 2300 Hz. The underestimation of predictions at higher frequencies and around absorption minima is often seen when testing additively manufactured specimens, especially those fabricated using the FDM technology [27,36,40]. This is because FDM printouts possess rough surfaces and other imperfections, such as uneven cross-section chiefly in the direction perpendicular to the printing direction, material shrinkage, and filament impurities, that usually intensify acoustic energy dissipation [40]. It was already demonstrated that the extrusion process itself and the

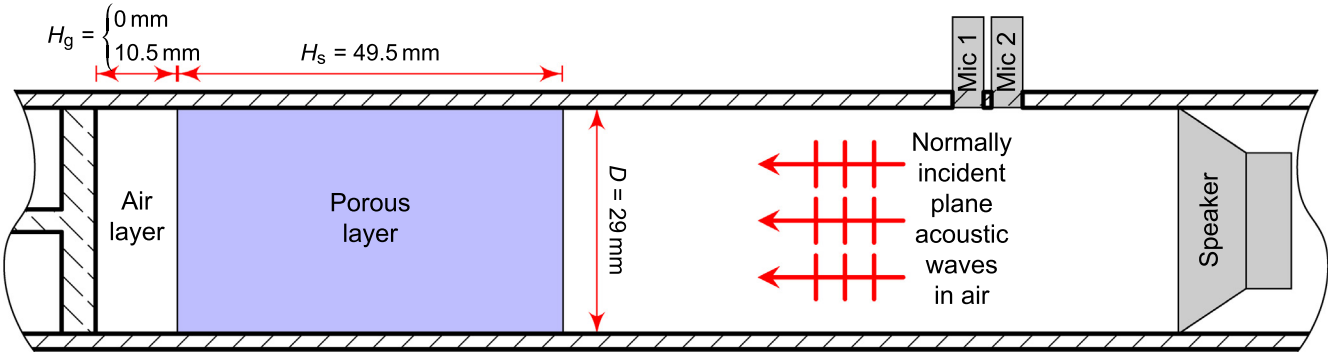

Fig. 6. Impedance tube configuration for normal incidence acoustic measurements.

Table 3
Data on the solved numerical problems and generated finite-element meshes.

Microgeometry	Problem dimension	Nodes	Elements	Degrees of freedom per analysis		
				thermal diffusion	electric conduction	viscous flow
$\vartheta = 0°$ (Fig. 1a)	1D	2	1	3	–	–
$\vartheta = 45°$ (Fig. b)	2D	642 341	1 277 334	2 560 320	2 560 320	5 762 133
$\vartheta = 30°$, zigzag, $l_{\text{fold}} = 1.25$ mm	2D	519 614	1 032 665	2 071 087	2 071 087	4 661 385
$\vartheta = 45°$, zigzag, $l_{\text{fold}} = 0.1$ mm	2D	478 244	952 170	1 908 308	1 908 308	4 294 685
$\vartheta = 45°$, zigzag, $l_{\text{fold}} = 0.5$ mm	2D	684 300	1 362 600	2 730 628	2 730 628	6 145 271
$\vartheta = 45°$, zigzag, $l_{\text{fold}} = 1.25$ mm (Fig. c)	2D	676 089	1 343 806	2 694 858	2 694 858	6 065 243
$\vartheta = 45°$, zigzag, $l_{\text{fold}} = 2$ mm	2D	656 364	1 302 975	2 614 559	2 614 559	5 884 910
$\vartheta = 45°$, zigzag, $l_{\text{fold}} = 3$ mm	2D	660 230	1 308 740	2 627 776	2 627 776	5 915 070
$\vartheta = 0°$, perforated (Fig. d)	3D	333 685	1 644 693	2 450 071	2 450 071	7 683 898
$\vartheta = 45°$, perforated (Fig. e)	3D	343 486	1 485 590	2 336 265	2 336 265	7 342 836

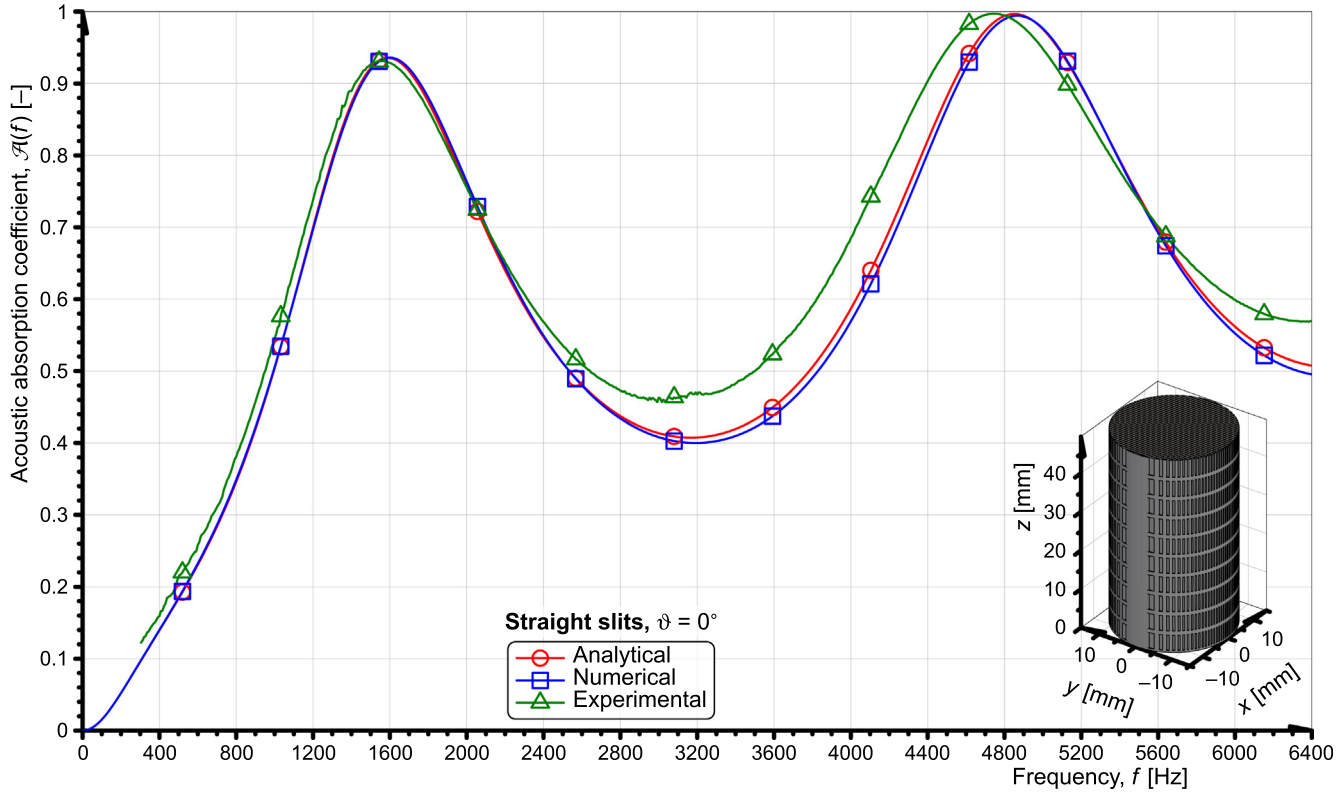

Fig. 8. Measured and predicted (analytically and numerically) normal incidence absorption coefficient spectra for a 49.5 mm-thick hard-backed layer of identical 0.3 mm-wide slits normal to the surface ($\vartheta = 0°$) separated by 0.4 mm-thick walls.

irregularity of the nozzle that the polymer filament is pulled by are the main two sources of these inherent defects which can be controlled to some extent by the selection of printing parameters and equipment [40].

Fig. 9 juxtaposes plots related to the slits inclined at $\vartheta = 45°$ to the surface of incidence. In this case, the idealised analytical and numerical results valid for infinitely wide (in other words, unbounded) material layer do not match the experimental data represented by green curves with triangles. This is because the relevant sample that the measurements were conducted on (see Fig. 4b) was bounded by a 29-mm diameter impedance tube and hence the depth of penetration of acoustic waves into the specimen was restricted to a small region close to the insonified surface. Fig. 10 precisely shows the wedge-shaped open porosity area (marked in blue) in the cylindrical sample, where slanted air-filled slits are accessible for sound waves propagating in the z-direction. The remaining part of the sample (not coloured) effectively reflects the waves instead of slowing them down. The correctness of this understanding is proved by the fact that the presented experimental absorption curves for the inclined slit configuration with and without the air gap left behind the sample are almost identical in the whole considered frequency range (compare the two nearly overlapping green curves having triangular markers in Fig. 9). If the diameter of the specimen had exceeded its thickness (that is $D_s > H_s$), sound waves would have reached the air gap and the curves would have therefore been distinguishable. Furthermore, the bigger the ratio D_s/H_s, the better the agreement between predictions and measurements because the impact of the closed porosity region on the overall energy dissipation within the sample, albeit always present, decreases with increasing D_s/H_s. Thus, it would be preferable to test such slitted microgeometries in large impedance tubes provided that a high quality congruent sample can be produced. Unfortunately, the larger the diameter of the tube, the easier it is for long and slender 3D printed solid strips to degenerate, spoiling the designed sample morphology. In compliance with their goal in this work, acoustic measure-

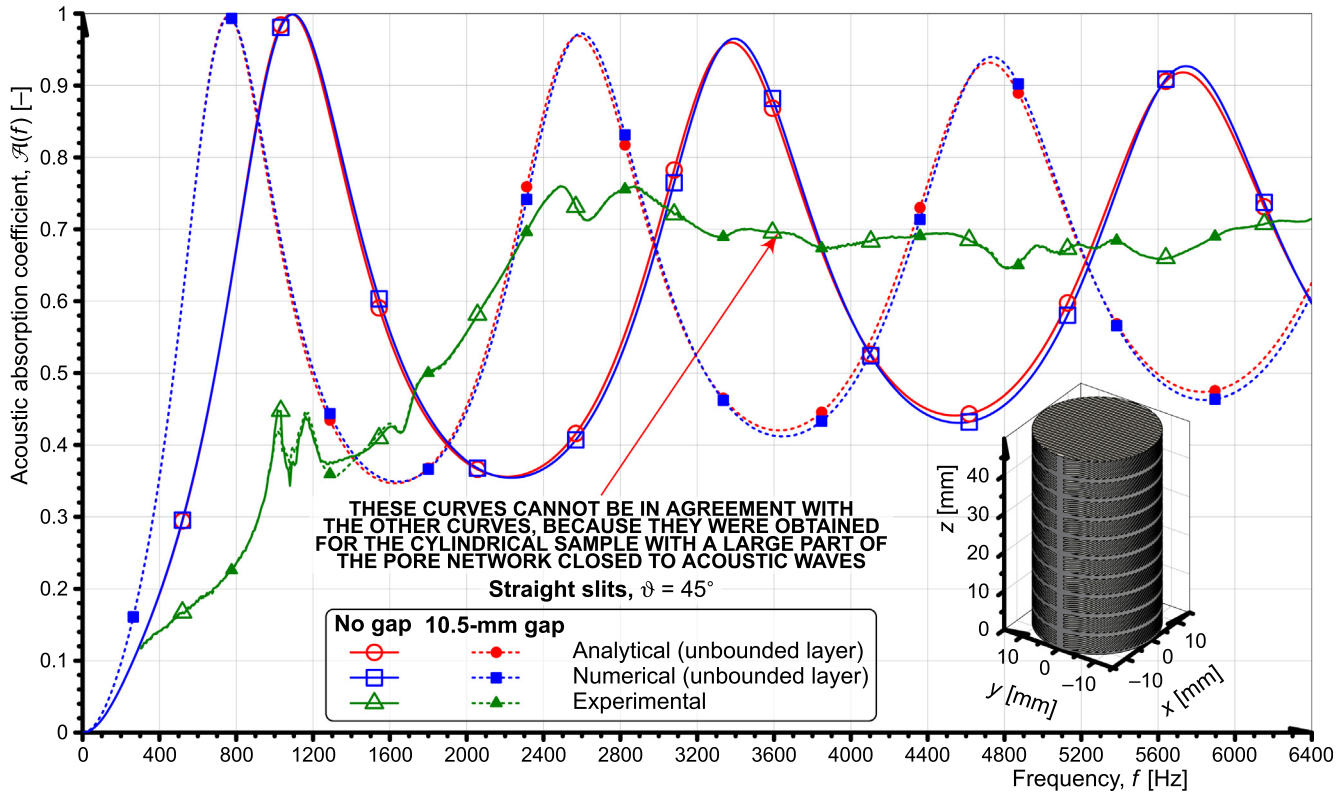

Fig. 9. Measured and predicted (analytically and numerically) normal incidence absorption coefficient spectra for a 49.5 mm-thick hard-backed layer of identical straight 0.3 mm-wide slits at 45 degrees to the surface ($\vartheta = 45^\circ$) and separated by 0.4 mm-thick walls, and the layer backed by a 10.5 mm-thick air gap. Included are results corresponding to both the cylindrical sample bounded by the walls of an impedance tube (the experimental curves) and the 'unbounded layer' (the analytical and numerical curves).

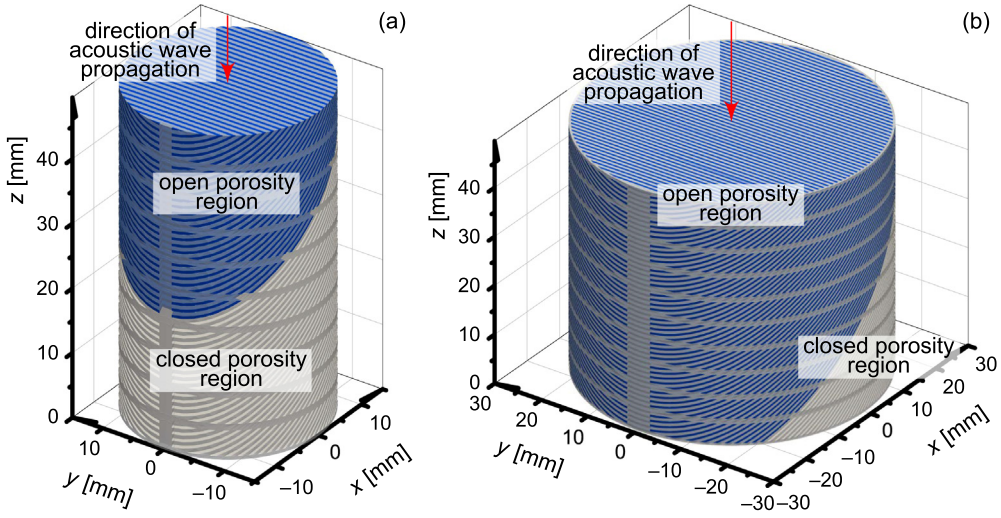

Fig. 10. Open (in blue) and closed (not coloured) porosity regions within the non-perforated sample of thickness $H_s = 49.5$ mm with slits inclined at $\vartheta = 45^\circ$ to the insonified surface—situation as in: (a) the 29-mm impedance tube used for acoustic testing ($D_s < H_s$); and (b) a 58-mm impedance tube ($D_s > H_s$). Because the slits within the sample are not mutually connected and the solid strips separating them are assumed perfectly rigid, the blue regions depict the only fragment of a hard-backed sample where sound waves can penetrate.

ments made on the 49.5 mm-thick specimen of diameter 29 mm revealed inappropriateness of the testing method to experimentally determining the sound absorption by straight inclined slits ($\vartheta = 45^\circ$) without interconnections. Nevertheless, the same microstructure in an unbounded material layer exhibits better acoustic performance than the slits aligned with the direction of incidence primarily due to the increased tortuosity [2,3] (its value doubles from 1 to 2). For example, the frequency of the quarter wavelength layer resonance in the sound absorption spectrum is lowered from 1.6 kHz to 1.1 kHz just by increasing the inclination angle from $\vartheta = 0^\circ$ to $\vartheta = 45^\circ$ (compare Fig. 8 to Fig. 9 with no gap results). In addition, there are three absorption peaks below 6 kHz instead of two, and the absorption at the first peak is predicted to be perfect for $\vartheta = 45^\circ$. These data indicate that the

hard-backed 49.5-mm layer with slits inclined at 45 degrees to the insonified surface is more efficient than the layer of the same thickness composed of slits normal to the surface.

The problem for inclined slits caused by the walls of the impedance tube is overcome by making the slits to zigzag through the sample. The zigzags allow pressure waves to propagate within the entire volume of the sample. For zigzag slits, the agreement between numerical calculations (the blue curve with squares in Fig. 11) and experimental results (the green curve with triangles in Fig. 11) is much better especially at absorption maxima. The discrepancies appearing around the minima of absorption are primarily because of the intrinsic printing defects (surface roughness, impurities, shrinkage, etc.) [34,36,40], but uncertainties related to slit size and shape, especially deep inside the sample, also seem to play an important role in here [70]. It is expected that the sparser the zigzag pattern in an unbounded layer, the smaller the discrepancies and the stronger the similarity between the straight inclined and zigzag materials in terms of the acoustic response. But notwithstanding that, the experimental pitfall associated with oblique slits still persists for zigzags to a small extent as it may happen that for certain D_s and l_{fold} pairs the slits near the impedance tube cylindrical wall are truncated. The study of the impact of l_{fold} on $\mathscr{A}(f)$ in the zigzag specimen (see Fig. 12) indeed shows that the smaller the distance between zigzag folds, l_{fold}, the more the acoustic absorption curve and the reference curve corresponding to straight slits and $\vartheta = 0^\circ$ are alike. In fact, the standard analytical formula for the dynamic viscous tortuosity $\alpha_{\text{A}}(\omega)$ in (6) is not capable of predicting the effect of folds. To make it applicable to the zigzag slits, one needs to incorporate into it a certain correction for the classic expression for the static viscous permeability, k_0, given by the Kozeny-Carman relationship [71]:

$$k_0 = \frac{1}{3}\phi w_s^2 \cos^2\vartheta\,. \tag{14}$$

Numerical studies using the finite-element method described in Sec. 2.2.3 show that the folded-slit structure with $\vartheta = 45^\circ$ tends to be more permeable as l_{fold} decreases (see Fig. 13). An empirical expression for k_0 is thus proposed that takes both ϑ and the unitless distance $l'_{\text{fold}} = l_{\text{fold}}/(1\,\text{m})$ into account:

$$k_0 = \frac{1}{3}\phi w_s^2 \frac{4000 l'_{\text{fold}} + 1}{4000 l'_{\text{fold}} + \cos^2\vartheta}\cos^2\vartheta \tag{15}$$

and entails the following modification to the formula (6):

$$\alpha_{\text{A}}(\omega) = \frac{4000 l'_{\text{fold}} + \cos^2\vartheta}{4000 l'_{\text{fold}} + 1}\cos^{-2}\vartheta\left(1 - \frac{\tanh(\lambda\sqrt{\text{i}})}{\lambda\sqrt{\text{i}}}\right)^{-1}. \tag{16}$$

The factor $(4000 l'_{\text{fold}} + 1)/(4000 l'_{\text{fold}} + \cos^2\vartheta)$ was established by fitting a curve to a series of k_0 numerical data points obtained for $\vartheta = 45^\circ$ and several fold distances l_{fold} with constraints on the limiting values. It is thereby ensured that for $l'_{\text{fold}} \to 0$ the viscous permeability $k_0 \to \frac{1}{3}\phi w_s^2 \equiv k_0|_{\vartheta=0^\circ}$, and for $l'_{\text{fold}} \to \infty$ the viscous permeability $k_0 \to \frac{1}{6}\phi w_s^2 \equiv k_0|_{\vartheta=45^\circ}$ as long as $\vartheta = 45^\circ$. For other inclination angles two analogous requirements are also satisfied. Fig. 13 compares the suggested analytical approximation (15) with the numerical reference results achieved for $\vartheta = 30^\circ$ and $\vartheta = 45^\circ$. Importantly, the numerical data is assumed to be converged as the relative change of k_0 with increasing density of a finite-element mesh is negligible. Formula (16) has been validated numerically for three fold distances, namely 0.1 mm,0.5 mm and 1.25 mm, as shown in Fig. 12, and has been verified for other inclination angles as well. For example, the analytical and numerical predic-

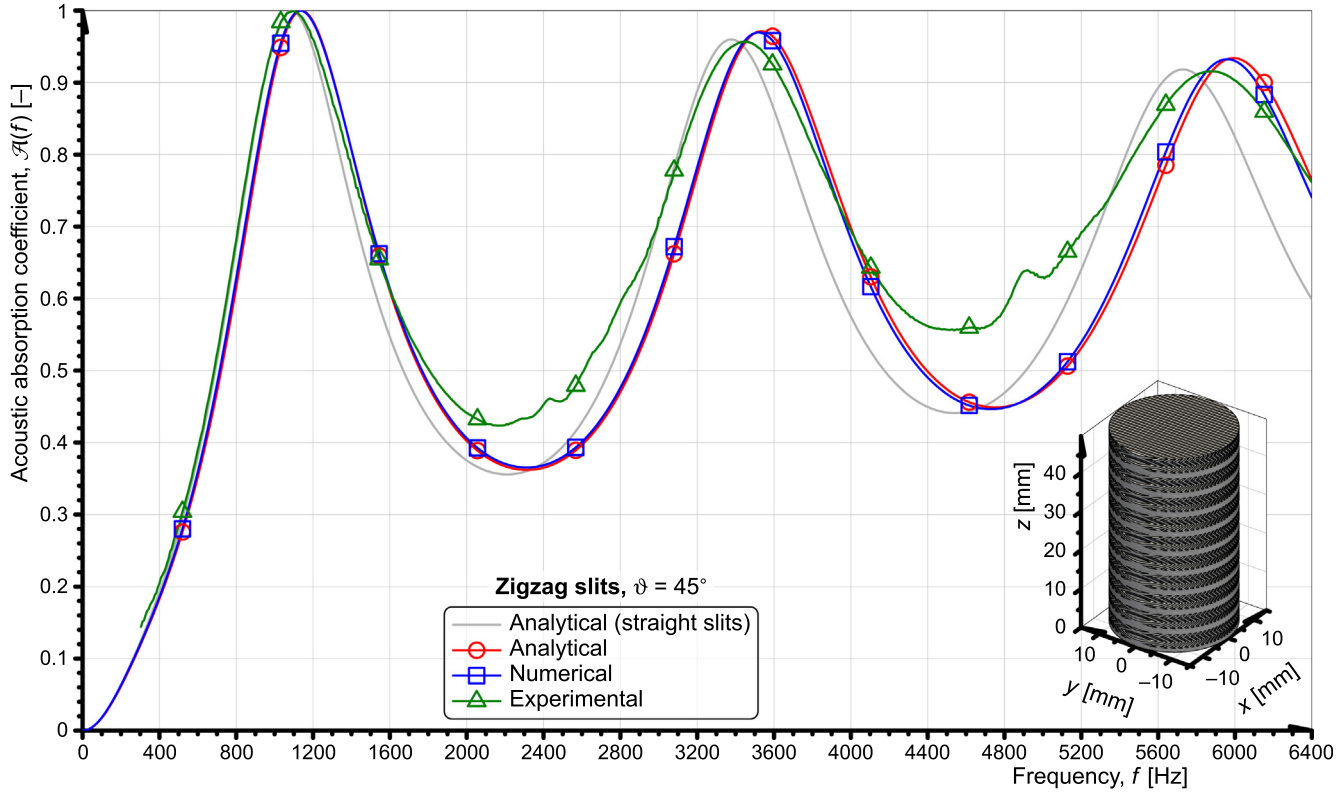

Fig. 11. Measured and predicted (analytically and numerically) normal incidence absorption coefficient spectra for a 49.5 mm-thick hard-backed layer of identical 0.3 mm-wide slits of a zigzag shape (with $\vartheta = 45^\circ$ and $l_{\text{fold}} = 1.25$ mm) separated by 0.4 mm-thick walls. The analytical result for the zigzag slits incorporates the proposed correction (15) for the static viscous permeability. Included for reference is the analytical result corresponding to the straight inclined slits in an 'unbounded layer' (see Fig. 9).

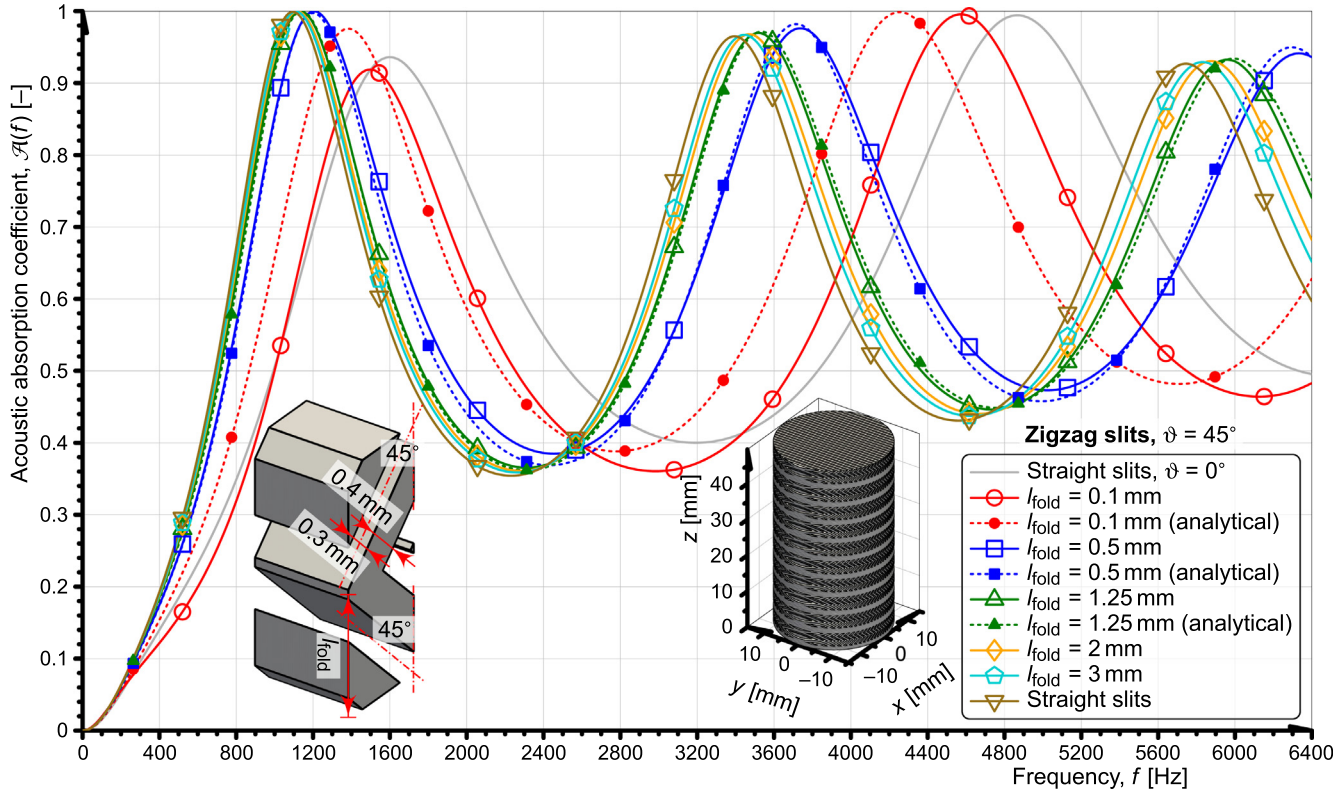

Fig. 12. Normal incidence acoustic absorption coefficient for a 49.5 mm-thick hard-backed layer composed of the zigzag slit pattern ($\vartheta = 45^\circ$) with different fold distances as well as straight slits normal and inclined at 45 degrees to the surface of incidence: a numerical study with three analytical solutions incorporating the proposed correction (15) for the static viscous permeability.

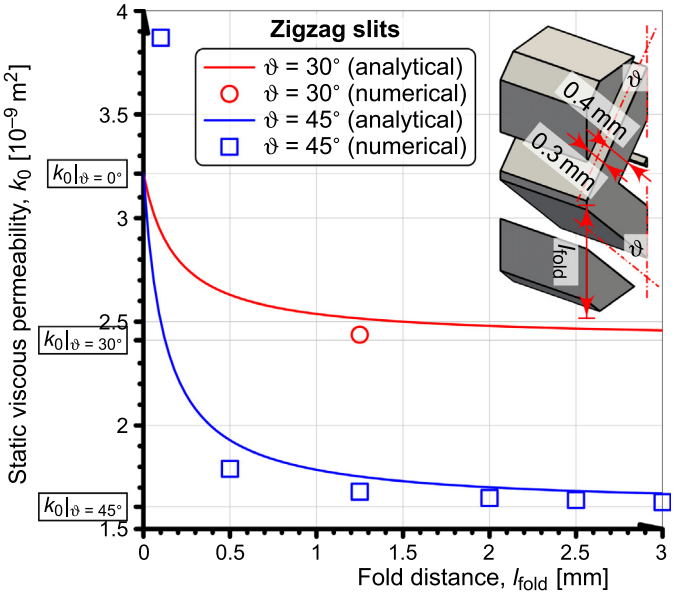

Fig. 13. The variation of the static viscous permeability, k_0, with the fold distance, l_{fold}, for the zigzag microgeometry: the proposed analytical approximation and numerical finite-element results. $k_0|_{\vartheta=0^\circ} \approx 3.214 \cdot 10^{-9}$ m^2 is the static viscous permeability for the structure with non-inclined straight slits, whereas $k_0|_{\vartheta=30^\circ} \approx 2.411 \cdot 10^{-9}$ m^2 and $k_0|_{\vartheta=45^\circ} \approx 1.607 \cdot 10^{-9}$ m^2 are the static viscous permeabilities for the case with straight slits inclined at $\vartheta = 30^\circ$ and $\vartheta = 45^\circ$ to the surface of incidence, respectively. A single numerical calculation only was made for 30 degrees angle of incidence.

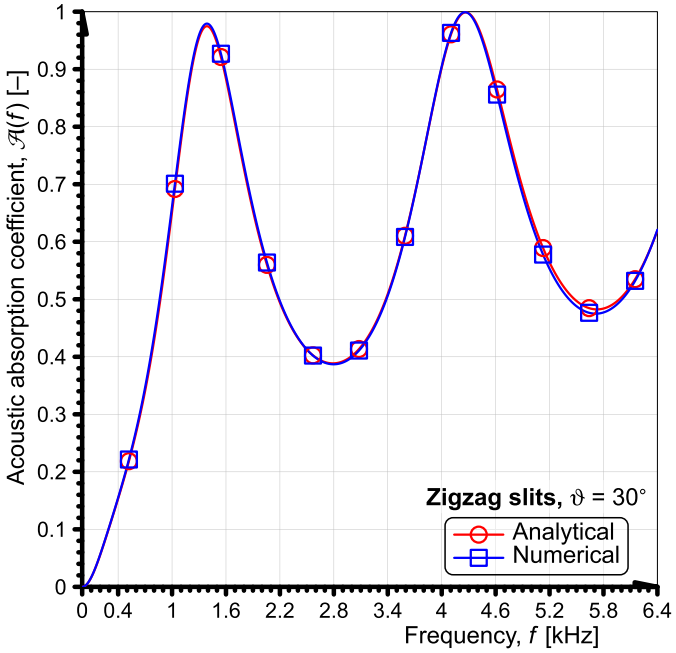

Fig. 14. Normal incidence sound absorption coefficient for a 49.5 mm-thick hard-backed material layer of the zigzag microgeometry with $\vartheta = 30^\circ$, $l_{fold} = 1.25$ mm, $2w_s = 0.3$ mm, and $2w_w = 0.4$ mm. The analytical result incorporates the proposed correction (15) for the static viscous permeability.

tions of the normal incidence sound absorption coefficient for zigzags with $\vartheta = 30^\circ$ plotted in Fig. 14 are almost identical.

Another method of opening to acoustic waves the entire inclined slit porous network within the sample shown in Fig. 4b is to perforate the slit walls thereby introducing a periodic

arrangement of cylindrical interconnections between slits. This solution has already proved efficient for materials other than slits [24–27,29]. The consequences of adding a regular $d_{\text{perf}} = 2\,\text{mm}$ perforation to the slitted geometry with $\vartheta = 0^\circ$ in the direction perpendicular to the slit plane are illustrated in Fig. 15. Numerical calculations (yellow curve with diamonds) show that in addition to the first absorption peak being lowered from 0.94 to 0.87, the second peak is a bit reduced and shifted to lower frequencies in comparison with the analytical solution for the non-perforated case (grey line). The analytical predictions based on the model with dead-end perforations (red curve with circles) seem most accurate in comparison with the experimental results (cyan curve with pentagons). On the other hand, the acoustic wave attenuation in the material predicted by the 'dead-end slits' analytical model that assumes cylindrical openings as the main pore network and slits as the dead-ends (blue curve with squares) is the strongest, but does not agree either with experimental data or with numerical and other theoretical results. The corresponding curve was obtained for the average h^{S} computed to be 1.96 mm instead of the limiting $l_{\text{perf}}/2 \approx 2.47\,\text{mm}$. The former more realistic value was evaluated as an average of local volume contributions pertaining to individual slit fragments within one period (in the z-direction) of the material using the expression:

$$h^{\text{S}} = \frac{1}{2}\frac{1}{2w_{\text{s}}l_{\text{perf}}N_{\text{slit}}}\sum_{i=1}^{N_{\text{slit}}}\frac{V_i}{N_{\text{perf},i}}, \tag{17}$$

where N_{slit} is the number of slits in a single layer, V_i and $N_{\text{perf},i}$ denote the volume of the saturating fluid (without the volume of the corresponding parts of the perforation channels) and the number of perforation channels it has an access to, respectively, within the i-th slit fragment. Fig. 16 depicts the actual geometry that served the computation, and the adopted numbering convention. It was observed that predictions of this model would have better agreement with the data from the alternative dead-end model employed (see the red curve with circles in Fig. 15) if the effective slit length were to be reduced further, for example to the value $h^{\text{S}} = l_{\text{perf}}/16$ (see the green curve with triangles in Fig. 15).

The introduction of cylindrical perforations of diameter d_{perf} and spacing l_{perf} also provides a way of making the microstructure with straight inclined slits suitable for impedance tube testing. Fig. 17 presents the absorption of sound within the sample with perforated inclined slits. The beneficial behaviour connected with the non-zero inclination angle and therefore the decreased effective sound speed in the medium is verified experimentally on the manufactured specimen and predicted using analytical and numerical models. Substantial quantitative discrepancies between the results that diminish at low frequencies and reflect the poor quality of the sample are observed. Again, the analytical curve based on the model with dead-end perforation (see Eqs 8 and 9) is closer to the numerical results than the curve based on the analogous model with $h^{\text{S}} = 1.96\,\text{mm}$ treating cylindrical channels as the main pore network in the computation of the equivalent bulk modulus, which describes the intensity of thermal phenomena in porous materials, but the differences between these two analytical approaches resolve if the effective slit length in the dead-end slit model is sufficiently small (see the curve obtained for $h^{\text{S}} = l_{\text{perf}}/16$ in Fig. 17). However, predictions assuming that the slits are the dead-end pores and the perforations are the main pores are in better agreement with the measured frequencies of the quarter wavelength resonances (compare the blue and cyan curves having square and pentagonal markers, respectively, in Fig. 17). The discrepancies between the dead-end pore predictions

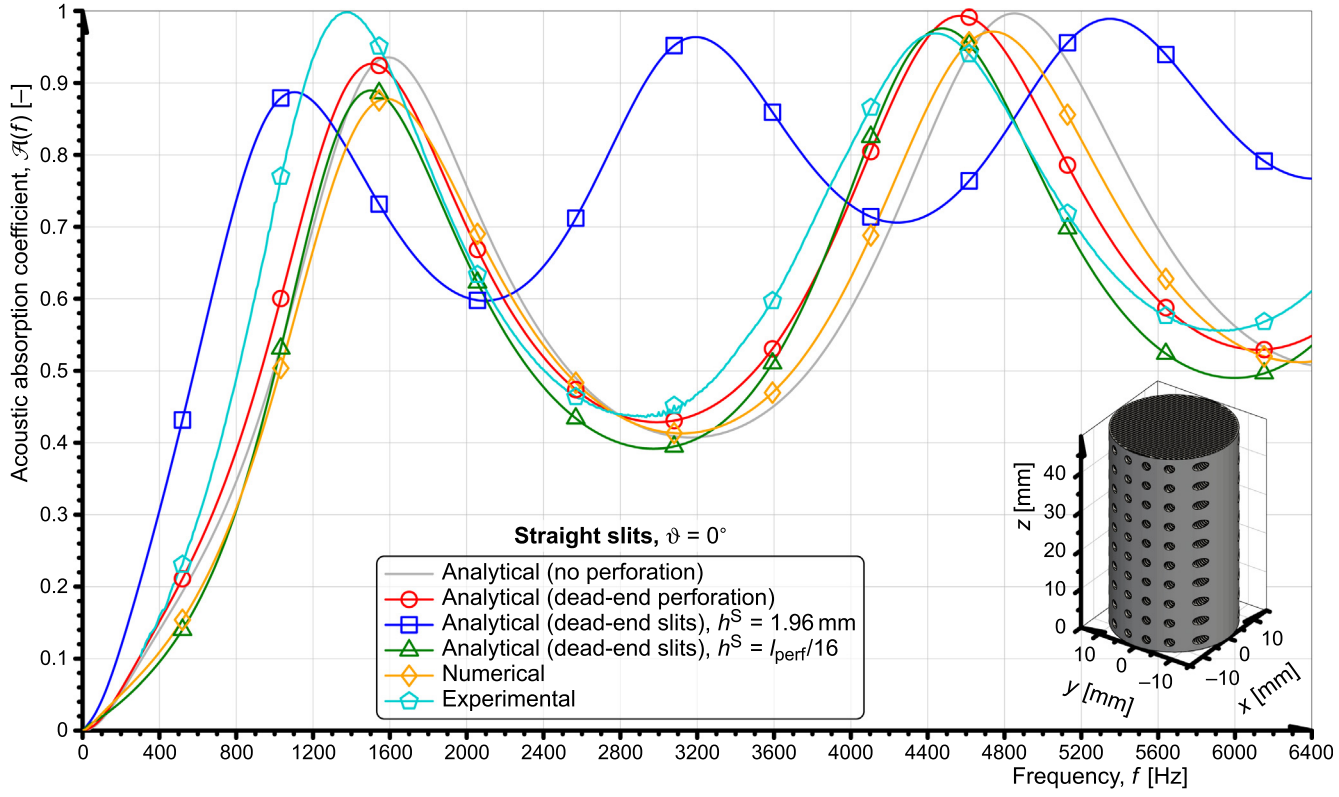

Fig. 15. Measured and predicted (analytically and numerically) normal incidence absorption coefficient spectra for a 49.5 mm-thick hard-backed layer of identical 0.3 mm-wide slits normal to the insonified surface ($\vartheta = 0^\circ$) and separated by 0.4 mm-thick walls without and with the 2-mm diameter cylindrical perforation ($l_{\text{perf}} \approx 4.95\,\text{mm}$) perpendicular to the slits. The effective slit length $h^{\text{S}} = 1.96\,\text{mm}$ was estimated from Eq. 17.

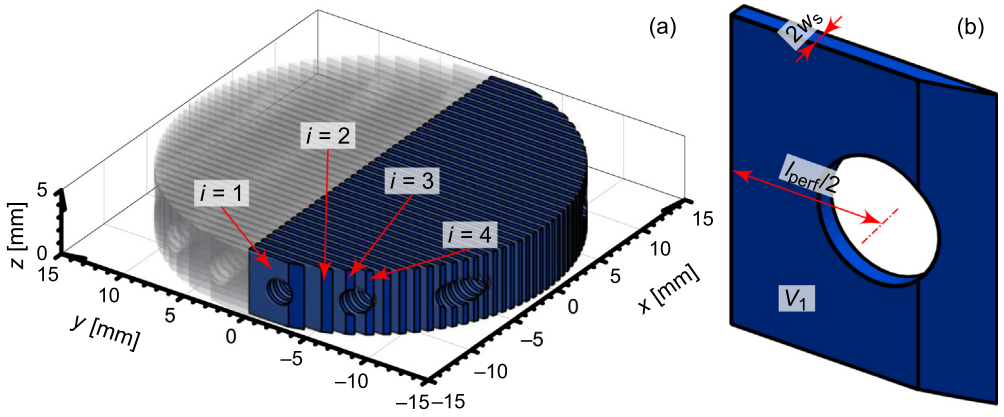

Fig. 16. Geometry used in the computation of h^S according to Eq. 17 for the perforated slitted sample with slits normal to the surface of incidence: (a) one period (in the z-direction) of the microgeometry with the blue region representing half of the fluid domain within the periodic layer due to sample symmetry, excluding the volume of the fluid saturating cylindrical perforation channels; (b) the first slit fragment ($i = 1$) of volume V_1 having connection to $N_{\text{perf},1} = 1$ perforation channels. The fluid domain in the presented layer consists of $N_{\text{slit}} = 41$ slits, where $N_{\text{perf},1} = 1, N_{\text{perf},2} = 1, N_{\text{perf},3} = 2, N_{\text{perf},4} = 2$, etc.

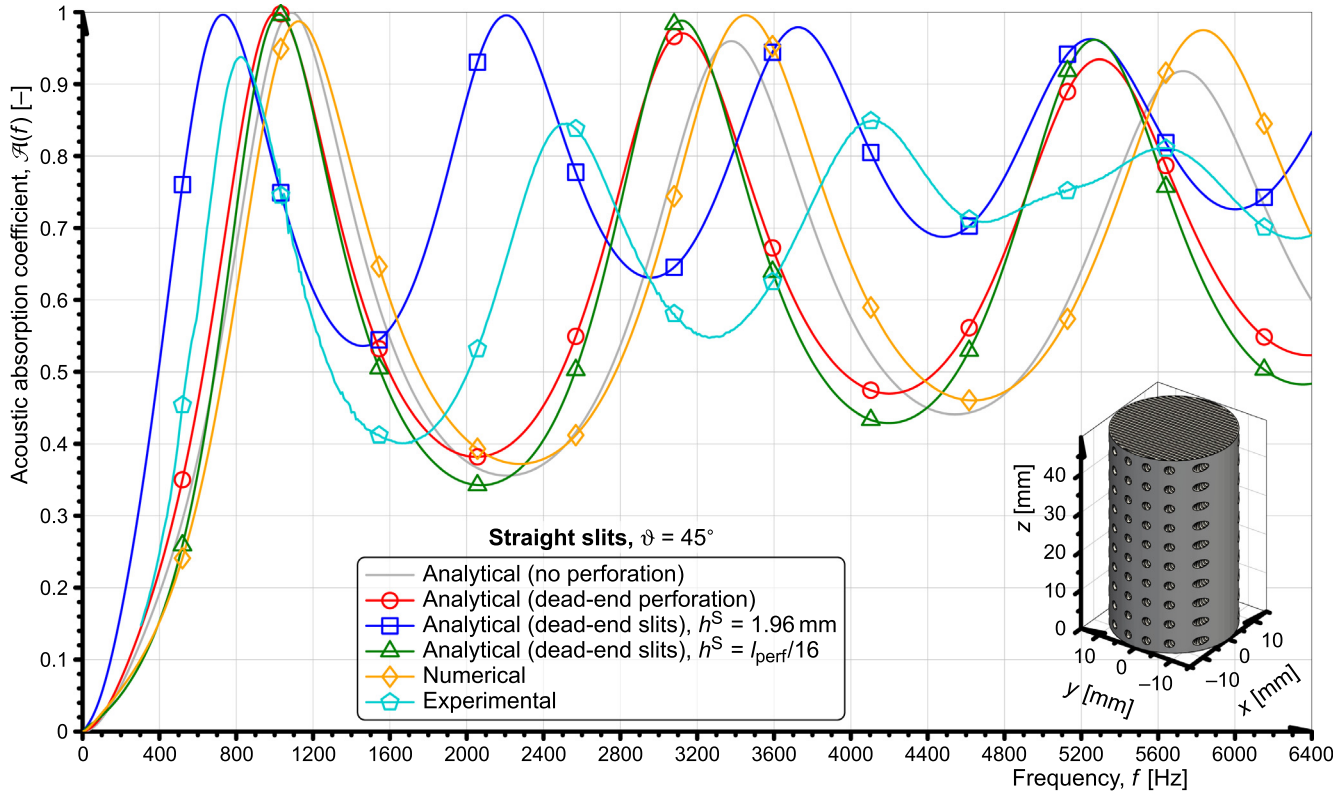

Fig. 17. Measured and predicted (analytically and numerically) normal incidence absorption coefficient spectra for a 49.5 mm-thick hard-backed layer of identical 0.3 mm-wide slits at 45 degrees to the insonified surface ($\vartheta = 45^\circ$) and separated by 0.4 mm-thick walls without and with the 2-mm diameter cylindrical perforation ($l_{\text{perf}} \approx 4.95$ mm) perpendicular to the direction of incidence. The effective slit length $h^S = 1.96$ mm was calculated from Eq. 17.

and other data are a consequence of the fact that the dead-end pore model allows only for thermal effects in the bulk modulus and does not include the variation of the equivalent density due to the presence of slit interconnections [56].

The manufactured slits are relatively wide and thus the corresponding static viscous permeabilities are high compared to those present in conventional acoustic porous materials, so one reports deep, wide valleys between sound absorption peaks. In principle, narrower slits (but only to some point) are needed to make absorption more broadband [3]. Given certain design constraints, the preferred absorption spectrum resulting from a simple slitted material can be approached by manipulating the slit characteristic parameters (width, porosity, and inclination angle), but there is also an optimum connected with the fact that too narrow slits tend to reflect incident acoustic waves rather than letting them penetrate the medium. Another way to enhance absorption is to incorporate slit partitions or perforations increasing the overall tortuosity of the microgeometry, or to make use of a distinct physical mechanism such as skeleton elasticity or pressure diffusion between slits and a porous skeleton [2].

The produced results confirm that the impedance tube examination of materials composed of straight inclined slits, even mutu-

ally linked, is difficult if not unfeasible. By studying the zigzag geometry one can replace a cumbersome oblique design by its close zigzag equivalent in terms of acoustic performance, which has some advantages like higher stiffness and capability of being tested in an impedance tube. Furthermore, the tendency to deform due to gravity and viscous attraction forces typical for long, straight, thin, inclined solid strips is no more present in the zigzags, because their local stability and stiffness resulting from frequent folds are increased. From this point of view, they are more reproducible and easier to manufacture. Finally, the proposed empirical correction formula for the static viscous permeability k_0 enables accurate analytical modelling of zigzag slits.

4. Conclusions

Manufacturing of efficient slitted sound-absorbing materials is not an easy task because of their small slit widths and spacings that require very high fabrication precision. Despite the production limitations, two low-cost additive manufacturing technologies were used to fabricate five slitted specimens yielding reliable data from measurements in an impedance tube. The normal incidence absorption of sound in the samples was predicted using analytical and semi-analytical approaches. The results lead to the following conclusions:

- The analytical models for the dynamic properties of homogenised slitted materials are often sufficiently accurate and much more efficient as compared with the partially numerical calculations incorporating the JCALP model.
- The analytical and numerical predictions generally agree well with the experimental results except for the microgeometry with slits inclined to the insonified surface and perforated with cylindrical channels, for which substantial discrepancies between predictions and measurements were reported. The discrepancies may be attributed to the difficulty in manufacturing long, narrow, inclined, straight slits that are uniform and not degenerated (note that the usage of zigzag slits, as proposed in this paper, seems to resolve this problem). In fact, visual inspection of the samples suggests that the slits inside the resin specimens tend to be a little wavy. This is probably where the limits of 3D printing become important. The twisted cross-section of slits, which is an imperfection of the manufacturing technology, influences the experimental results so that the agreement between predictions and measurements is poorer for the case of the LCD samples—the absorption maxima are moved to lower frequencies due to the locally increased tortuosity. Moreover, the dead-end pore model does not allow for narrow pores, in which viscous effects are important, which heavily contributes to the observed discrepancies.
- Despite large discrepancies in predictions of the sound absorption coefficient spectra obtained for the most complex perforated sample with oblique slits, the general qualitative character of the experimental curves is followed by the analytical and numerical predictions. The differences get smaller at low frequencies.
- Little gain in absorption was achieved by the applied perforation. Modifying its diameter, shape or spacing may provide more significant benefit in terms of acoustic wave energy dissipation.
- The proposed enhanced expression for the static viscous permeability in the analytical formulas for straight slits enables this standard model to be applicable to zigzag structures. The improvement takes into account both the inclination angle and the distance between consecutive zigzag folds.
- Regardless of a serious effort put into sample preparation using budget additive manufacturing technologies, some microgeometries may not be suited to impedance tube measurements or simply difficult to fabricate precisely.

Producibility and performance of slitted sound absorbers were confronted in the paper. This is an important study because slits and narrow channels in general often constitute an essential part of optimised systems designed to effectively absorb sounds with frequencies far below 1000 Hz. These solutions typically require 3D printing of the material microstructure which shares the same difficulties as reported and discussed in this contribution. Because of the proposed enhanced analytical prediction of the sound propagation in zigzag slits and the investigated modelling of perforated slits using the dead-end models, it contains information about a fast alternative to relatively slow and computationally demanding numerical calculations for these geometries and can pave the way for more elaborate theoretical considerations.

Despite the difficulties of producing a good quality sample, zigzags were shown to absorb acoustic waves as efficiently as inclined straight slits do. Similar manufacturing and experimental challenges seem to pertain to other promising designs like narrow labyrinthine channels, slits with sinusoidal width variation, periodically non-uniform slits or partitioned structures [2,3] as well. One idea to circumvent some of the identified problems is to make measurements in a quadrilateral impedance tube which can be a potential extension of the work. Anyway, the findings of the paper indicate that an enormous acoustic potential of simple shapes including straight narrow slits still needs to be explored.

Data availability

The raw data required to reproduce these findings can be obtained by contacting the corresponding author.

Declaration of Competing Interest

The authors declare that they have no known competing financial interests or personal relationships that could have appeared to influence the work reported in this paper.

Acknowledgements

The financial support of the project number 2020/37/N/ST8/04071: “Impact of the 3D printing process on the acoustic properties of porous materials”, financed by the National Science Centre (NCN), Poland, is gratefully acknowledged. T.G. Zieliński gratefully acknowledges the financial support from the project “Sound-absorbing composites: coupled acoustic energy dissipation mechanisms, multiscale modelling and prototyping”, financed under Grant Agreement No. 2021/41/B/ST8/04492 by the National Science Centre (NCN), Poland.

Appendix A. Hybrid micro–macro approach

The macroscopic acoustic properties of a porous material depend on its microstructure and thickness. There exist direct and hybrid methods to quantify the effect of microgeometry being incorporated into the properties of a homogenised fluid equivalent to the porous medium [54]. The hybrid technique utilises scaling functions such as the one given by the JCALP model and used in this work. In any case, the dynamic tortuosities, which define $\varrho_{\mathrm{eq}}(\omega)$ and $K_{\mathrm{eq}}(\omega)$ by Eqs 1 and 2, are computed numerically on a representative unit cell domain with the porosity, ϕ, and thermal characteristic length, Λ', equal:

$$\phi = \frac{\int_{\Omega_f} d\Omega}{\int_{\Omega_c} d\Omega}, \qquad \Lambda' = 2\frac{\int_{\Omega_f} d\Omega}{\int_{\Gamma_{sf}} d\Gamma},$$

where Ω_c is the entire unit cell region, Ω_f is the fluid domain in the unit cell, and Γ_{sf} is the solid–fluid interface. In the direct approach one calculates $\alpha_N(\omega)$ and $\alpha\prime_N(\omega)$ by solving two harmonic problems for each frequency. On the other hand, the hybrid strategy is by far less expensive as it relies on a scaling function (for example, the JCALP model) that relates $\alpha_N(\omega)$ and $\alpha\prime_N(\omega)$ to a set of static macroscopic parameters describing the microgeometry of the porous network. It is therefore not needed to perform computations for each frequency, but for the JCALP model (Eqs 12 and 13) one can predict $\alpha_N(\omega)$ and $\alpha\prime_N(\omega)$ using the necessary parameters $(\phi, k_0, k\prime_0, \alpha_\infty, \alpha_0, \alpha\prime_0, \Lambda, \Lambda')$ determined purely from the microstructure morphology and three asymptotic behaviours [54]. The 'viscous' parameters at $\omega \to 0$ are evaluated as:

$$k_0 = \phi\left\langle \hat{\mathbf{k}}_0 \cdot \mathbf{e} \right\rangle_f \quad \text{and} \quad \alpha_0 = \frac{\left\langle \hat{\mathbf{k}}_0 \cdot \hat{\mathbf{k}}_0 \right\rangle_f}{\left(\left\langle \hat{\mathbf{k}}_0 \cdot \mathbf{e} \right\rangle_f\right)^2}$$

from the dimensionless Stokes problem:

$$\begin{aligned} -\Delta\hat{\mathbf{k}}_0 + \nabla\psi_0 &= \mathbf{e} && \text{in } \Omega_f, \\ -\nabla\cdot\hat{\mathbf{k}}_0 &= 0 && \text{in } \Omega_f, \\ \hat{\mathbf{k}}_0 &= \mathbf{0} && \text{on } \Gamma_{sf}, \end{aligned}$$

where $\hat{\mathbf{k}}_0$ is the velocity vector scaled to the unit of m^2, ψ_0 is the scaled (to the unit of m) pressure, $\mathbf{e}$ is the unit vector consistent with the direction of acoustic wave propagation ($\mathbf{e} = [0, 0, 1]$ in this paper), and $\langle\cdot\rangle_f \equiv \int_{\Omega_f}(\cdot)\,d\Omega / \int_{\Omega_f} d\Omega$ is the averaging operator over the fluid volume. The 'inertial' parameters at $\omega \to \infty$ are calculated as:

$$\alpha_\infty = \frac{1}{\langle \mathbf{E}\cdot\mathbf{E}\rangle_f}, \qquad \Lambda = \frac{\int_{\Omega_f} \mathbf{E}\cdot\mathbf{E}\,d\Omega}{\int_{\Gamma_{sf}} \mathbf{E}\cdot\mathbf{E}\,d\Gamma},$$

where $\mathbf{E} = \mathbf{e} - \nabla q$ is the dimensionless vector field, and q is the solution to the Laplace equation:

$$\begin{aligned} \Delta q &= 0 && \text{in } \Omega_f, \\ \nabla q\cdot\mathbf{n} &= \mathbf{e}\cdot\mathbf{n} && \text{on } \Gamma_{sf} \end{aligned}$$

with $\mathbf{n}$ being the normal unit vector pointing outwards the fluid domain. Similarly, the Poisson equation:

$$\begin{aligned} -\Delta\hat{k}_0 &= 1 && \text{in } \Omega_f, \\ \hat{k}_0 &= 0 && \text{on } \Gamma_{sf}, \end{aligned}$$

where $\hat{k}_0$ is the scaled (to the unit of m^2) temperature, is solved to estimate the 'thermal' parameters from the following expressions:

$$k\prime_0 = \phi\left\langle \hat{k}_0 \right\rangle_f, \qquad \alpha\prime_0 = \frac{\left\langle (\hat{k}_0)^2 \right\rangle_f}{\left(\left\langle \hat{k}_0 \right\rangle_f\right)^2}.$$

In some of the above equations the units near zeros are omitted for better readability.

References

[1] J.-F. Allard, N. Atalla, Propagation of sound in porous media: Modelling sound absorbing materials, second ed., John Wiley & Sons, 2009. https://doi.org/10.1002/9780470747339.

[2] K. Attenborough, Microstructures for lowering the quarter wavelength resonance frequency of a hard-backed rigid-porous layer, Appl. Acoust. 130 (2018) 188–194, https://doi.org/10.1016/j.apacoust.2017.09.022.

[3] K. Attenborough, Macro- and micro-structure designs for porous sound absorbers, Appl. Acoust. 145 (2019) 349–357, https://doi.org/10.1016/j.apacoust.2018.10.018.

[4] W. Chen, T. Chen, F. Xin, X. Wang, X. Du, T.J. Lu, Modeling of sound absorption based on the fractal microstructures of porous fibrous metals, Mater. Des. 105 (2016) 386–397, https://doi.org/10.1016/j.matdes.2016.05.076.

[5] C. Perrot, F. Chevillotte, R. Panneton, Bottom-up approach for microstructure optimization of sound absorbing materials, J. Acoust. Soc. Am. 124 (2) (2008) 940–948, https://doi.org/10.1121/1.2945115.

[6] S. Ren, F. Xin, T.J. Lu, C. Zhang, A semi-analytical model for the influence of temperature on sound propagation in sintered metal fiber materials, Mater. Des. 134 (2017) 513–522, https://doi.org/10.1016/j.matdes.2017.09.007.

[7] T.G. Zieliński, Microstructure representations for sound absorbing fibrous media: 3D and 2D multiscale modelling and experiments, J. Sound Vib. 409 (6) (2017) 112–130, https://doi.org/10.1016/j.jsv.2017.07.047.

[8] C. Lagarrigue, J.P. Groby, O. Dazel, V. Tournat, Design of metaporous supercells by genetic algorithm for absorption optimization on a wide frequency band, Appl. Acoust. 102 (2016) 49–54, https://doi.org/10.1016/j.apacoust.2015.09.011.

[9] J.P. Groby, C. Lagarrigue, B. Brouard, O. Dazel, V. Tournat, B. Nennig, Using simple shape three-dimensional rigid inclusions to enhance porous layer absorption, J. Acoust. Soc. Am. 136 (2014) 1139–1148, https://doi.org/10.1121/1.4892760.

[10] W. Sun, B. Pan, X. Song, H. Xiao, J. Zhou, D. Sui, A novel sound absorber design of nanofibrous composite porous material, Mater. Des. 214 (2022) 1–12, https://doi.org/10.1016/j.matdes.2022.110418. 110418.

[11] D.W. Wang, Z.H. Wen, C. Glorieux, L. Ma, Sound absorption of face-centered cubic sandwich structure with micro-perforations, Mater. Des. 186 (2020) 1–10, https://doi.org/10.1016/j.matdes.2019.108344. 108344.

[12] J. de Priester, A. Aulitto, I. Lopez Arteaga, Frequency stop-band optimization in micro-slit resonant metamaterials, Appl. Acoust. 188 (2022) 1–12, https://doi.org/10.1016/j.apacoust.2021.108552. 108552.

[13] S. Gasser, F. Paun, Y. Bréchet, Absorptive properties of rigid porous media: Application to face centered cubic sphere packing, J. Acoust. Soc. Am. 117 (4) (2005) 2090–2099, https://doi.org/10.1121/1.1863052.

[14] C.Y. Lee, M.J. Leamy, J.H. Nadler, Acoustic absorption calculation in irreducible porous media: A unified computational approach, J. Acoust. Soc. Am. 126 (4) (2009) 1862–1870, https://doi.org/10.1121/1.3205399.

[15] T.G. Zieliński, Microstructure-based calculations and experimental results for sound absorbing porous layers of randomly packed rigid spherical beads, J. Appl. Phys. 116 (3) (2014) 1–17, https://doi.org/10.1063/1.4890218. 034905.

[16] C. Perrot, F. Chevillotte, M.T. Hoang, G. Bonnet, F.X. Bécot, L. Gautron, A. Duval, Microstructure, transport, and acoustic properties of open-cell foam samples: Experiments and three-dimensional numerical simulations, J. Appl. Phys. 111 (1) (2012) 1–16, https://doi.org/10.1063/1.3673523. 014911.

[17] O. Doutres, M. Ouisse, N. Atalla, M. Ichchou, Impact of the irregular microgeometry of polyurethane foam on the macroscopic acoustic behavior predicted by a unit-cell model, J. Acoust. Soc. Am. 136 (4) (2014) 1666–1681, https://doi.org/10.1121/1.4895695.

[18] J.H. Park, K.S. Minn, H.R. Lee, S.H. Yang, C.B. Yu, S.Y. Pak, C.S. Oh, Y.S. Song, Y.J. Kang, J.R. Youn, Cell openness manipulation of low density polyurethane foam for efficient sound absorption, J. Sound Vib. 406 (2017) 224–236, https://doi.org/10.1016/j.jsv.2017.06.021.

[19] J.H. Park, S.H. Yang, H.R. Lee, C.B. Yu, S.Y. Pak, C.S. Oh, Y.J. Kang, J.R. Youn, Optimization of low frequency sound absorption by cell size control and multiscale poroacoustics modeling, J. Sound Vib. 397 (2017) 17–30, https://doi.org/10.1016/j.jsv.2017.03.004.

[20] M. Álvarez-Láinez, M.A. Rodríguez-Pérez, J.A. de Saja, Acoustic absorption coefficient of open-cell polyolefin-based foams, Mater. Lett. 121 (2014) 26–30, https://doi.org/10.1016/j.matlet.2014.01.061.

[21] V.H. Trinh, V. Langlois, J. Guilleminot, C. Perrot, Y. Khidas, O. Pitois, Tuning membrane content of sound absorbing cellular foams: Fabrication, experimental evidence and multiscale numerical simulations, Mater. Des. 162 (2019) 345–361, https://doi.org/10.1016/j.matdes.2018.11.023.

[22] F. Chevillotte, C. Perrot, E. Guillon, A direct link between microstructure and acoustical macro-behavior of real double porosity foams, J. Acoust. Soc. Am. 134 (6) (2013) 4681–4690, https://doi.org/10.1121/1.4824842.

[23] V.H. Nguyen, E. Rohan, S. Naili, Multiscale simulation of acoustic waves in homogenized heterogeneous porous media with low and high permeability contrasts, Int. J. Eng. Sci. 101 (2016) 92–109, https://doi.org/10.1016/j.ijengsci.2015.12.004.

[24] P. Bai, X. Yang, X. Shen, X. Zhang, Z. Li, Q. Yin, G. Jiang, F. Yang, Sound absorption performance of the acoustic absorber fabricated by compression and microperforation of the porous metal, Mater. Des. 167 (2019) 1–14, https://doi.org/10.1016/j.matdes.2019.107637. 107637.

[25] F. Chevillotte, C. Perrot, R. Panneton, Microstructure based model for sound absorption predictions of perforated closed-cell metallic foams, J. Acoust. Soc. Am. 128 (4) (2010) 1766–1776, https://doi.org/10.1121/1.3473696.

[26] K.C. Opiela, T.G. Zieliński, T. Dvorák, S. Kúdela Jr., Perforated closed-cell metal foam for acoustic applications, in: Proc. of e-Forum Acusticum 2020, Lyon, France, 2020, pp. 2879–2886. https://doi.org/10.48465/fa.2020.0925.

[27] K.C. Opiela, T.G. Zieliński, T. Dvorák, S. Kúdela Jr., Perforated closed-cell aluminium foam for acoustic absorption, Appl. Acoust. 174 (2021) 1–17, https://doi.org/10.1016/j.apacoust.2020.107706. 107706.

[28] W. Zhai, X. Yu, X. Song, L.Y.L. Ang, F. Cui, H.P. Lee, T. Li, Microstructure-based experimental and numerical investigations on the sound absorption property of open-cell metallic foams manufactured by a template replication technique, Mater. Des. 137 (2018) 108–116, https://doi.org/10.1016/j.matdes.2017.10.016.

[29] J. Carbajo, J.M. Molina-Jordá, L.P. Maiorano, N.X. Fang, Sound absorption of macro-perforated additively manufactured media, Appl. Acoust. 182 (2021) 1–8, https://doi.org/10.1016/j.apacoust.2021.108204. 108204.
[30] S. Deshmukh, H. Ronge, S. Ramamoorthy, Design of periodic foam structures for acoustic applications: Concept, parametric study and experimental validation, Mater. Des. 175 (2019) 1–14, https://doi.org/10.1016/j.matdes.2019.107830. 107830.
[31] W. Johnston, B. Sharma, Additive manufacturing of fibrous sound absorbers, Addit. Manuf. 41 (2021) 1–22, https://doi.org/10.1016/j.addma.2021.101984. 101984.
[32] K.C. Opiela, T.G. Zieliński, Adaptation of the equivalent-fluid model to the additively manufactured acoustic porous materials, in: M. Ochmann, M. Vorländer, J. Fels (Eds.), Proc. of the 23rd International Congress on Acoustics: Integrating 4th EAA Euroregio 2019, Deutsche Gesellschaft für Akustik, Berlin, Germany, 2019, pp. 1216–1223, https://doi.org/10.18154/RWTH-CONV-239799.
[33] T.G. Zieliński, Pore-size effects in sound absorbing foams with periodic microstructure: Modelling and experimental verification using 3D printed specimens, in: P. Sas, D. Moens, A. van de Walle (Eds.), Proc. of ISMA2016 International Conference on Noise and Vibration Engineering/USD2016 International Conference on Uncertainty in Structural Dynamics, Katholieke Universiteit Leuven, Department of Mechanical Engineering, Heverlee, Belgium, 2016, pp. 95–104.
[34] T.G. Zieliński, K.C. Opiela, P. Pawłowski, N. Dauchez, T. Boutin, J. Kennedy, D. Trimble, H. Rice, B. Van Damme, G. Hannema, R. Wróbel, S. Kim, S. Ghaffari Mosanenzadeh, N.X. Fang, J. Yang, B. Briere de la Hosseraye, M.C.J. Hornikx, E. Salze, M.A. Galland, R. Boonen, A. Carvalho de Sousa, E. Deckers, M. Gaborit, J.P. Groby, Reproducibility of sound-absorbing periodic porous materials using additive manufacturing technologies: Round robin study, Addit. Manuf. 36 (2020) 1–24, https://doi.org/10.1016/j.addma.2020.101564. 101564.
[35] K.C. Opiela, M. Rak, T.G. Zieliński, A concept demonstrator of adaptive sound absorber/insulator involving microstructure-based modelling and 3D printing, in: W. Desmet, B. Pluymers, D. Moens, W. Rottiers (Eds.), Proc. of ISMA2018 International Conference on Noise and Vibration Engineering/USD2018 International Conference on Uncertainty in Structural Dynamics, Katholieke Universiteit Leuven, Department of Mechanical Engineering, Heverlee, Belgium, 2018, pp. 1091–1104.
[36] K.C. Opiela, T.G. Zieliński, Microstructural design, manufacturing and dual-scale modelling of an adaptable porous composite sound absorber, Compos. Part B: Eng. 187 (2020) 1–13, https://doi.org/10.1016/j.compositesb.2020.107833. 107833.
[37] D. O'Connor, J. Kennedy, An evaluation of 3D printing for the manufacture of a binaural recording device, Appl. Acoust. 171 (2021) 1–8, https://doi.org/10.1016/j.apacoust.2020.107610. 107610.
[38] X. Zhang, K. Zhang, L. Zhang, W. Wang, Y. Li, R. He, Additive manufacturing of cellular ceramic structures: From structure to structure-function integration, Mater. Des. 215 (2022) 1–25, https://doi.org/10.1016/j.matdes.2022.110470. 110470.
[39] J. Boulvert, T. Cavalieri, J. Costa-Baptista, L. Schwan, V. Romero-García, G. Gabard, E.R. Fotsing, A. Ross, J. Mardjono, J.-P. Groby, Optimally graded porous material for broadband perfect absorption of sound, Journal of Applied Physics 126 (17) (2019) 1–15 175101. https://doi.org/10.1063/1.5119715.
[40] J. Boulvert, J. Costa-Baptista, T. Cavalieri, M. Perna, E.R. Fotsing, V. Romero-García, G. Gabard, A. Ross, J. Mardjono, J.P. Groby, Acoustic modeling of micro-lattices obtained by additive manufacturing, Appl. Acoust. 164 (2020) 1–9, https://doi.org/10.1016/j.apacoust.2020.107244. 107244.
[41] E.R. Fotsing, A. Dubourg, A. Ross, J. Mardjono, Acoustic properties of periodic micro-structures obtained by additive manufacturing, Appl. Acoust. 148 (2019) 322–331, https://doi.org/10.1016/j.apacoust.2018.12.030.
[42] M.D. Guild, V.M. García-Chocano, W. Kan, J. Sánchez-Dehesa, Acoustic metamaterial absorbers based on multilayered sonic crystals, J. Appl. Phys. 117 (11) (2015) 1–14, https://doi.org/10.1063/1.4915346. 114902.
[43] Y. Tang, S. Ren, H. Meng, F. Xin, L. Huang, T. Chen, C. Zhang, T.J. Lu, Hybrid acoustic metamaterial as super absorber for broadband low-frequency sound, Scient. Rep. 7 (2017) 1–10, https://doi.org/10.1038/srep43340. 43340.
[44] M. Nori, R. Venegas, Sound propagation in porous materials with annular pores, J. Acoust. Soc. Am. 141 (6) (2017) 4642–4651, https://doi.org/10.1121/1.4986939.
[45] A. Aulitto, A. Hirschberg, Ines Lopez Arteaga, Influence of geometry on acoustic end-corrections of slits in microslit absorbers, J. Acoust. Soc. Am. 149 (5) (2021) 3073–3085, https://doi.org/10.1121/10.0004826.
[46] S.W. Ren, H. Meng, F.X. Xin, T.J. Lu, Sound absorption enhancement by thin multi-slit hybrid structures, Chin. Phys. Lett. 32 (1) (2015) 1–4, https://doi.org/10.1088/0256-307x/32/1/014302. 014302.
[47] S.W. Ren, H. Meng, F.X. Xin, T.J. Lu, Ultrathin multi-slit metamaterial as excellent sound absorber: Influence of micro-structure, Journal of Applied Physics 119 (1) (2016) 1–8 014901. https://doi.org/10.1063/1.4938735.
[48] T.G. Zieliński, F. Chevillotte, E. Deckers, Sound absorption of plates with micro-slits backed with air cavities: Analytical estimations, numerical calculations and experimental validations, Appl. Acoust. 146 (2019) 261–279, https://doi.org/10.1016/j.apacoust.2018.11.026.
[49] J. Carbajo, S. Ghaffari Mosanenzadeh, S. Kim, N.X. Fang, Multi-layer perforated panel absorbers with oblique perforations, Appl. Acoust. 169 (2020) 1–7, https://doi.org/10.1016/j.apacoust.2020.107496. 107496.
[50] I. Bashir, S. Taherzadeh, K. Attenborough, Surface waves over periodically-spaced rectangular strips, J. Acoust. Soc. Am. 134 (6) (2013) 4691–4697, https://doi.org/10.1121/1.4824846.
[51] K.C. Opiela, T.G. Zieliński, K. Attenborough, Manufacturing, modeling, and experimental verification of slitted sound absorbers, in: W. Desmet, B. Pluymers, D. Moens, S. Vandemaele (Eds.), Proc. of ISMA2020 International Conference on Noise and Vibration Engineering/USD2020 International Conference on Uncertainty in Structural Dynamics, Katholieke Universiteit Leuven, Department of Mechanical Engineering, Heverlee, Belgium, 2020, pp. 409–420.
[52] K.C. Opiela, T.G. Zieliński, K. Attenborough, Impedance-tube characterisation of additively manufactured slitted sound absorbers, in: SAPEM2020+1 — 6th Symp. on the Acoustics of Poro-Elastic Materials, Purdue University, West Lafayette, USA, 2021.
[53] T.D. Ngo, A. Kashani, G. Imbalzano, K.T.Q. Nguyen, D. Hui, Additive manufacturing (3D printing): A review of materials, methods, applications and challenges, Compos. Part B: Eng. 143 (2018) 172–196, https://doi.org/10.1016/j.compositesb.2018.02.012.
[54] T.G. Zieliński, R. Venegas, C. Perrot, M. Červenka, F. Chevillotte, K. Attenborough, Benchmarks for microstructure-based modelling of sound absorbing rigid-frame porous media, J. Sound Vib. 483 (2020) 1–38, https://doi.org/10.1016/j.jsv.2020.115441. 115441.
[55] A. Dell, A. Krynkin, K.V. Horoshenkov, The use of the transfer matrix method to predict the effective fluid properties of acoustical systems, Appl. Acoust. 182 (2021) 1–10, https://doi.org/10.1016/j.apacoust.2021.108259. 108259.
[56] P. Leclaire, O. Umnova, T. Dupont, R. Panneton, Acoustical properties of air-saturated porous material with periodically distributed dead-end pores, J. Acoust. Soc. Am. 137 (4) (2015) 1772–1782, https://doi.org/10.1121/1.4916712.
[57] D.L. Johnson, J. Koplik, R. Dashen, Theory of dynamic permeability and tortuosity in fluid-saturated porous media, J. Fluid Mech. 176 (1987) 379–402, https://doi.org/10.1017/S0022112087000727.
[58] Y. Champoux, J.F. Allard, Dynamic tortuosity and bulk modulus in air-saturated porous media, J. Appl. Phys. 70 (4) (1991) 1975–1979, https://doi.org/10.1063/1.349482.
[59] S.R. Pride, A.F. Gangi, F.D. Morgan, Deriving the equations of motion for porous isotropic media, J. Acoust. Soc. Am. 92 (6) (1992) 3278–3290, https://doi.org/10.1121/1.404178.
[60] S.R. Pride, F.D. Morgan, A.F. Gangi, Drag forces of porous-medium acoustics, Phys. Rev. B 47 (9) (1993) 4964–4978, https://doi.org/10.1103/PhysRevB.47.4964.
[61] D. Lafarge, Comments on "Rigorous link between fluid permeability, electric conductivity, and relaxation times for transport in porous media", Phys. Fluids A 5 (2) (1993) 500–502, https://doi.org/10.1063/1.858873.
[62] D. Lafarge, P. Lemarinier, J.F. Allard, V. Tarnow, Dynamic compressibility of air in porous structures at audible frequencies, J. Acoust. Soc. Am. 102 (4) (1997) 1995–2006, https://doi.org/10.1121/1.419690.
[63] FreeCAD (version 0.19.2), https://www.freecadweb.org/, accessed: 2022-04-14.
[64] Slic3r Prusa (version 1.38.5), https://www.prusa3d.com/page/prusaslicer_424/, accessed: 2022-04-14.
[65] Z-SUITE (version 2.18.1), https://zortrax.com/software/, accessed: 2022-04-14.
[66] ISO 10534-2, Acoustics — Determination of sound absorption coefficient and impedance in impedance tubes — Part 2: Transfer-function method, ISO standard, International Organisation for Standardization, Case postale 56, CH-1211 Genève 20, Switzerland (Nov. 1998).
[67] M.S. Alnæs, J. Blechta, J. Hake, A. Johansson, B. Kehlet, A. Logg, C. Richardson, J. Ring, M.E. Rognes, G.N. Wells, The FEniCS Project version 1.5, Archive of Numerical Software 3 (100) (2015) 9–23. https://doi.org/10.11588/ans.2015.100.20553.
[68] O.C. Zienkiewicz, R.L. Taylor, J.Z. Zhu, The finite element method: Its basis and fundamentals, 7th Edition., Butterworth-Heinemann, 2013, https://doi.org/10.1016/B978-1-85617-633-0.00019-8.
[69] C. Geuzaine, J.F. Remacle, Gmsh: A 3-D finite element mesh generator with built-in pre- and post-processing facilities, Int. J. Numer. Meth. Eng. 79 (11) (2009) 1309–1331, https://doi.org/10.1002/nme.2579.
[70] V.H. Trinh, J. Guilleminot, C. Perrot, On the sensitivity of the design of composite sound absorbing structures, Mater. Des. 210 (2021) 1–16, https://doi.org/10.1016/j.matdes.2021.110058. 110058.
[71] P.C. Carman, Flow of gases through porous media, Butterworths Scientific Publications, London, 1956.